Diffuse Reflectance Spectroscopy

Using a Monte-Carlo method to determine chromophore concentrations of tissue

LUND
UNIVERSITY

Lisa Kobayashi Frisk

J. Axelsson, S. Andersson-Engels

Department of Physics
Lund University

This dissertation is submitted for the degree of
Master of Science

Atomic Physics Division May 2016

Acknowledgements

I would like to acknowledge my supervisor, Johan Axelsson, and co-supervisor, Stefan Andersson-Engels, for their guidance and helpful insight throughout the duration of this thesis. Thank you for all of the hours you have spent discussing the project with me and always making me feel welcome to the group. I feel very privileged to have had such supportive supervisors, and I appreciate all of the effort that you have put into supervising me.

Additionally, I would like to thank Nina Reistad for giving me some additional insight and for also lending me some of her equipment, my lab partner Hasti for helping me in the lab and keeping me company, and finally other friends and office mates who have made this year a great experience!

Lisa Kobayashi Frisk

Popular Science Description

8.2 million people around the world died of cancer in 2014 [1], and in Sweden cancer rates have been increasing steadily for the past 20 years [2]. Since cancer is such a common disease, cancer research is a very 'hot' topic. Researchers are working hard not only to develop more efficient treatments, but also to develop better diagnostic techniques. In this work, light is used to develop a diagnostic method that could be used during cancer treatment.

The anatomy of tumour tissue changes when the tumour grows, and also while the tumour is being treated. More specifically, the amount of blood and oxygen in the tumour tissue changes. If the amount of blood and oxygen in tissue could be determined accurately, this would provide invaluable information when treating tumours. Light is able to be used to determine the amount of blood or oxygen in tissue because the way light travels through tissue depends on what is inside of it. In order to understand how light can be used to determine the composition of tissue one can consider runners running a course. One runner runs up a mountain at high speed and the other runs a flat course at low speed. If we see the runners after a certain distance, we can determine which course each runner took by analysing their heart rates, amount of sweat produced, etc. The runners here are analogous to light, and the course they travel is analogous to tissue. If we shine light onto a tissue and then detect light that exits the tissue a certain distance away, we can determine what was in that tissue by observing how the spectrum of the light changed after propagating through it. This is the basic principle of the technique used in this work, known as Diffuse Reflectance Spectroscopy.

In order to use Diffuse Reflectance Spectroscopy to determine the composition of tissue, one must be able to theoretically model the propagation of light through tissue. One model, known as the diffusion equation, is easy to implement and commonly used. However, the diffusion equation cannot correctly model all tissue types and experimental setups. Another model, known as Monte Carlo, is more difficult to implement but is less limiting than the diffusion equation. In this work, both the diffusion equation and Monte Carlo are used to try to extract the composition of solutions (referred to as liquid phantoms) that mimick the optical properties of biological tissue. The results, despite some errors, indicate a good outlook for using Diffuse Reflectance Spectroscopy as a diagnostic method during cancer

therapy.

Supervisors: **Johan Axelsson**, **Stefan Andersson-Engels**

Master's Thesis 60 hp in Photonics, 2016

Atomic Physics Division, Lund University

Abstract

In this work, inverse diffusion equation and Monte Carlo models are used in conjunction with diffuse reflectance spectroscopy to develop a protocol for evaluating the chromophore compositions of tissue mimicking liquid phantoms. A novel two spectrometer system is used which provides real time calibration of any intensity fluctuations of the light source. The calibration of this setup is investigated in detail. In order to analyse the limitations of the two theoretical models (diffusion equation and Monte Carlo), two optical probes with source-detector separations of 0.5 and 2 mm are used. The final evaluated fittings of whole blood, deoxygenated haemoglobin, oxygenated haemoglobin concentrations and μ_s values are relatively good. Possible approaches for improving the experimental data are discussed. The Monte Carlo method is shown to give better results than the diffusion equation for short probe designs, as expected from theory. However, for longer probe designs, the diffusion theory evaluates the data better. This is likely due to worse planar fitting of the Monte Carlo look-up table at long source-detector separations. In general however, the results are promising and indicate good prospects for using this system on real biological systems.

Self-Reflection

Throughout this thesis work, I have not only learned new theoretical concepts but also learned how to work independently on a research project and critically analyse my work. I started working on this project in September by carrying out a thorough literature search on the theoretical background of diffuse optics, the optical properties of different chromophores, some biology of what sort of chromophores commonly exist in blood, etc. I also read extensively about how different research groups have employed both Monte Carlo and the Diffusion Equation in a diffuse reflectance spectroscopy setup. This literature search gave me a solid background on the research topic and gave me direction on how to approach my project.

This project required me to have sound knowledge of theoretical models of light propagation in media. I then had to apply the theory in order to develop my own evaluation protocols. Through this process I became comfortable using MATLAB, which is something I have no formal experience in. I did not just apply the theoretical models to my work, but I also worked a lot with understanding the limitations and flaws of the models and critically analysed them.

Working with the experimental data is where I really learned many new things and pushed myself to new limits. In the biomedical field there are a lot of sources of error, and it is sometimes not possible to control all of them. For example, the values of μ_s, the SDS, ε of different chromophores etc. are not well known. In order to experimentally verify all of these sources of error would be a thesis of its own. Because of all of these different sources of error, it is not trivial to pinpoint what is effecting any 'bad' results. Working on this project made me go through my experimental data analytically.

Regular weekly meetings with my main supervisor where I presented the results and work that I had done over the past week kept me organised and responsible for my work and progress. These meetings also helped me practice communicating my thoughts orally to my supervisor.

Table of contents

Nomenclature

Roman Symbols

g	Anisotropy Factor
n	Refractive Index

Greek Symbols

ε_i	Extinction Coefficient
μ_a	Absorption Coefficient
μ_s	Scattering Coefficient
μ_s'	Reduced Scattering Coefficient

Acronyms / Abbreviations

DE	Diffusion Equation
FM	Forward Model
Hb	Haemoglobin
HbO_2	oxy-Haemoglobin
HHb	deoxy-Haemoglobin
IL	Intralipid® 20%
MC	Monte Carlo
MCML	Monte Carlo Multi-Layer
metHb	met-Haemoglobin

mfp mean free path

SDS Source-Detector separation

Chapter 1

Introduction

Cancer is one of the leading causes of death worldwide, with 14 million reported cases in 2012 [1]. This number is expected to rise in the future, and therefore research in cancer treatment is of major importance. Several treatment modalities exist, one being radionuclide therapy. In radionuclide therapy, a radiopharmaceutical, or radionuclide, is delivered to the patient's bloodstream. Antibodies are attached to the radionuclide so that it binds to cancerous cells. The ionising radiation released by the radionuclide then kills the cancerous cells, while healthy cells remain unaffected [3].

In order to properly administer radionuclide therapy, it is important to have some knowledge of the composition of the cancerous tissue. This work will use Diffuse Reflectance Spectroscopy (DRS) to develop an evaluation protocol for determining the composition of biological tissue. In the future, this evaluation protocol will be used to assess treatment response through changes in the tissue composition during radionuclide therapy.

In this introduction, the underlying concepts of DRS, and its specific applications in radionuclide therapy will be discussed.

1.1 Diffuse Reflectance and Diffuse Reflectance Spectroscopy

DRS refers to the study of the spectra of diffusely reflected photons, rather than specularly reflected photons. Specular reflectance refers to the reflectance of light off of a flat, polished surface (e.g. mirror). It is described by Snell's Law and the Fresnel Equations, where the reflected intensity of the light depends on the angle of incidence of the light. This is shown in Figure 1.1a

Diffuse reflectance on the other hand, refers to reflectance where the angular distribution of the reflected radiation is independent of the incident angle. Perfectly diffuse reflectors are

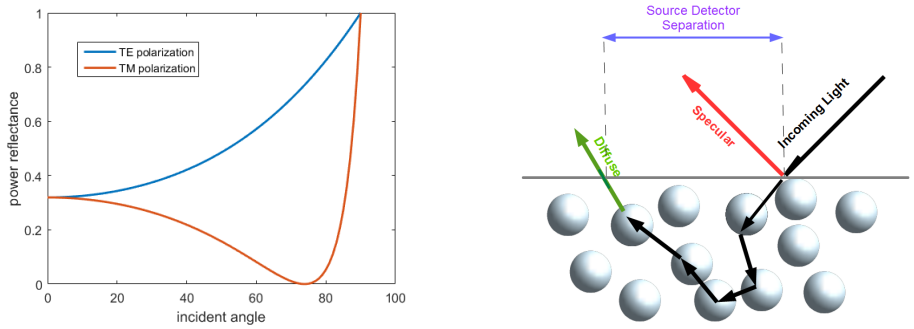

(a) *(b)*

Fig. 1.1 a: The power reflectance of the TE and TM polarized waves with $n_1 = 1$ and $n_2 = 3.56$ as calculated using the Fresnel Equations. b: Specular and diffuse reflectance

known as Lambertian surfaces. An example of a nearly perfect diffuse reflector is Spectralon® diffuse reflectance material. Spectralon® has >99% reflectance over the UV-VIS-NIR range [4].

When light propagates through tissue, it can experience scattering and absorption events due to its constituent particles. After several scattering events, the light that exits the tissue will be nearly isotropic and is therefore considered to be diffusely reflected light. The difference between specular and diffuse reflectance is illustrated in Figure 1.1b. Incoming light (black) is reflected both specularly (red) and diffusely (green). For diffuse reflectance, the source-detector separation (SDS) is defined as the distance between the incoming source beam and the point at which the diffusely reflected light is collected.

The path that the diffusely reflected light takes when propagating through tissue depends on the tissue's optical properties. Therefore, a diffuse reflectance spectrum contains information on the tissue's optical properties. Optical properties, in turn, are directly related to the tissue composition. This forms the foundation of DRS.

1.2 Motivation

As mentioned previously, this work encompasses the development of an evaluation protocol for determining the composition of biological tissue using DRS. This evaluation protocol will be eventually used in conjunction with radionuclide therapy of cancer. Knowledge of tissue composition is important during radionuclide therapy since the outcome of the therapy is linked to the concentration of blood and oxygen in the tumour. A more detailed background on this is given in the following text.

Hypoxia, the condition in which the amount of oxygen available in a system is so low as to compromise biological function, is known to affect the success of cancer treatment. Normally oxygenated, normoxic, cells can turn hypoxic due to two different effects:

1. The distances between nutritive blood vessels and cells can increase with tumour growth causing a lack of diffusion of oxygen to far away cells.

2. The growth of the tumour can result in irregular blood vessel structure which temporarily restricts the amount of oxygen available to nearby cells.

Hypoxia can be measured by both direct oxygenation measurements and measurements of the concentration of blood in the tissue. Low blood concentrations indicate compromised vascular structure which induces hypoxia.

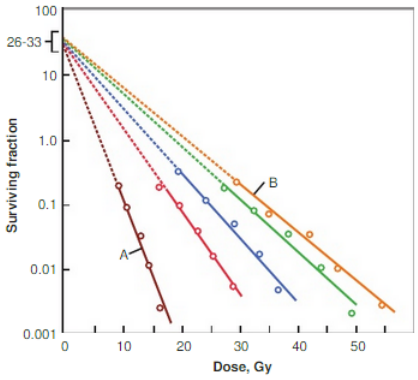

Fig. 1.2 The survival fraction for cells exposed to varying doses of radiation. The line marked A is a well-oxygenated cell while B is a very hypoxic cell. The remaining lines have varying oxygenations between these two extremes [5].

Of interest in this thesis is the effect of hypoxia in tumours on the outcome of radionuclide therapy. It is known that the radiation dose required to kill a certain fraction of cells is related to the oxygenation of the cells (Figure 1.2). During radionuclide therapy, a certain radiation dose will effectively kill normoxic cells however, hypoxic cells could survive. Remaining hypoxic cells can reoxygenate through different pathways[1]. Reoxygenation of the hypoxic cells leads to regeneration of the tumour, resulting in a cycle of ineffective radionuclide therapy.

DRS has been used by several groups to determine tissue composition in conjunction to cancer therapy [7–9]. In 2009 Vishwanath et al.[8], studied the oxygenation in a group of

[1] including induction of the protein HIF-1, and genetic adaptation of the cells to the hypoxic environment [6].

34 mice which were inoculated with cancerous cells. The oxygenation of the tumours was measured using a DRS system (wavelengths between 480 and 650 nm measuring reflectances at a depth greater than 0.3 mm). The diffuse reflections of the light were recorded, and using light-propagation simulations[2], the blood and oxygen concentrations were determined. It was found that the oxygen concentration increased for all animals after radiotherapy. A portion of the animals responded well to the treatment with no recurrences after 90 days, and were classified as Complete Responders (CR's). Another group had no tumour recurrences during the 90 days post treatment and were therefore classified as Partial Responders (PR's). The group found that using their method, it is possible to differentiate CR's from PR's and non responders early on in the treatment (5 days) by looking at the increase in the blood oxygen saturation levels.

1.3 Purpose and Aims

An efficient, cheap, and non-invasive method of determining the oxygenation distribution within a tumour would allow for a more effective prescription of radionuclide therapy as well as a better estimation of a patient's prognosis. To this end, an experimental DRS setup is designed and an evaluation protocol for determining the composition of liquid phantoms based on theoretical light-propagation models is developed. The liquid phantoms used have similar optical properties to biological tissue. A general overview of the specific aims of the thesis is given below.

1. Measuring penetration depth of light: An obvious drawback of using light to determine tissue composition is that tissue is not transparent. Therefore, the depth that the light penetrates the tissue is limited. In order to determine the penetration depth of light in tissue, light penetration depths were simulated for different wavelengths, source and detector fiber separations, and optical properties of tissue.

2. Phantom preparation, DRS measurements, and calibration: Liquid phantoms mimicking the optical properties of tissue were created by mixing blood, Intralipid®, and water. Calibrating the DRS spectra of the phantoms is not straight-forward and several methods have been used by different groups [10–12]. In this thesis, various calibration methods have been developed and tested.

3. Evaluating diffuse reflectance spectra: The main aim of this thesis is to extract the composition of the liquid phantoms using DRS. After calibrating the spectra, evaluation

[2]The theory behind this will be discussed in the following chapter.

protocols based on two different light propagation models are developed. The accuracy to which these two methods can evaluate the composition of the phantoms is compared.

Chapter 2

Theoretical Background

In order to evaluate a diffuse reflectance spectrum, one must be able to theoretically simulate light propagation in tissue. There are different theoretical models which do this, and these models are known as forward models (FM). A forward model calculates a theoretical reflectance spectrum using variable parameters corresponding to the tissue composition. Light propagation in tissue is described mathematically by the Radiation Transport Equation (RTE). In this thesis two approaches for solving the RTE are considered: the Diffusion Equation, which solves the RTE by approximating an isotropic light source, and a Monte Carlo method which solves the RTE stochastically. After a forward model is calculated, the difference between the experimental spectrum and the forward model is determined. Using a minimisation algorithm, the difference between these two spectra is successively minimised by updating the variable parameters of the forward model. Once the difference is minimised the variable parameters that minimised the difference are extracted. This is known as the inverse problem.

In this chapter, the theoretical background of the scattering and absorption properties of light in tissue, the RTE and its solutions (Diffusion Equation and Monte Carlo) will be discussed. The background of the inverse problem will also be given.

2.1 Propagation of Light in Tissue

Animal tissue is made of various chromophores, or molecules that interact with light: haemoglobin of different types (e.g. HbO_2 and HHb), lipid, water, etc. When light interacts with these chromophores, two events can occur:

1. A photon can be absorbed by the chromophore

2. A photon can be scattered, i.e., re-emitted by the chromophore.

The absorption and scattering properties of these chromophores are what transports light through tissue. The scattering and absorption events are probabilistic, and the probabilities of the events occurring are contained in the scattering and absorption coefficients (μ_s and μ_a) respectively. The length that a photon travels between each scattering or absorption event is referred to as its mean free path (mfp). It is defined mathematically as $1/(\mu_s + \mu_a)$.

2.1.1 Scattering

When an EM wave interacts with a particle, or scatterer, the electron orbits of the molecules within that particle are disturbed periodically with the same frequency as the EM wave. These induced dipole moments result in EM radiation emitted from the molecules. This process is known generally as scattering [13].

The complete solutions to how EM radiation is scattered is given by either Rayleigh of Mie theories depending on the size of the scatterer. Rayleigh theory is valid for scatterers much smaller than the wavelength of the incident radiation, while Mie theory is valid when describing scattering from spherical particles on the same order of magnitude as the wavelength of the incident radiation. The constituents of biological tissue are commonly approximated to particles and therefore the scattering properties of these tissues can be described using Rayleigh and Mie theories.

Scattering and Reduced Scattering Coefficients: μ_s & μ_s'

Physically, the scattering coefficient, μ_s, is the probability of a photon being scattered at some angle per unit length. Therefore, $1/\mu_s$ is the mean free path between each anisotropic scattering event.

When light is diffuse, i.e. when scattering dominates over absorption, another scattering coefficient can be introduced. This scattering coefficient is referred to as the reduced scattering coefficient. The reduced scattering coefficient is related to the scattering coefficient through the following relation:

$$\mu_s'(\lambda) = (1-g)\mu_s. \tag{2.1}$$

The reduced scattering coefficient differs from the scattering coefficient in that it describes isotropic scattering. The difference between the two coefficients, μ_s and μ_s' is shown in Figure 2.1. The short pink arrows represent scattering events with a mean free path equal to

$1/\mu_s$. The green arrow on the other hand represents one scattering event with a mean free path equal to $1/\mu_s'$.

Therefore, the value $1/\mu_s'$, describes not only the length between each scattering event but also the isotropy of the light after scattering determined by the anisotropy factor, g. It is defined by $g = \langle \cos\theta \rangle = \int_{-1}^{1} p(\cos\theta)\cos\theta \mathrm{d}\theta$, where $\langle\theta\rangle$ is the average deflection angle of the scattering events, and $p(\cos\theta)$ is the scattering phase function. In biomedical optics, the scattering phase function is often approximated by the Henyey-Greenstein function given by [14]:

$$p(\cos\theta) = \frac{1}{2}\frac{1-g^2}{(1+g^2-2g\cos\theta)^{3/2}}. \qquad (2.2)$$

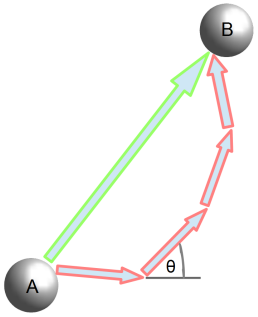

Fig. 2.1 Illustration of scattering of a photon.

Biological tissue is a forward scattering tissue and a commonly cited value for the anisotropic factor is approximately $g = 0.8$. The anisotropy factor of mouse skin was measured by Jaques et.al to be 0.74 ± 0.07 [15]. Although the discrepancy between various sources is large, the trend of data taken on anisotropy by various groups suggests a tendency of increasing g with increasing wavelength [16].

The complete expression for the reduced scattering coefficient is:

$$\mu_s'(\lambda) = a(f_{Ray}(\frac{\lambda}{\lambda_0})^{-4} + (1-f_{Ray})(\frac{\lambda}{\lambda_0})^{-b_{Mie}}). \qquad (2.3)$$

Equation 2.3, contains two terms distinguishing the separate contributions of Rayleigh and Mie scattering. The factor f_{Ray} indicates the fraction of scattering events characterized as Rayleigh scattering. The remaining coefficients, a, and b are the scattering amplitude and scattering power respectively. The scattering power is a scaling factor equal to $\mu_s(\lambda_0)$. The scattering power, b, takes values 4 and b_{Mie} corresponding to the correct values required by Rayleigh and Mie scattering theories respectively.

2.1.2 Absorption

Absorption refers to the absorption of light by a molecule whose electronic energy levels have an energy difference equal to the energy of the light[1]:

$$\Delta E = h\frac{c}{\lambda}. \tag{2.4}$$

The main absorbers in biological tissue are blood[2], water, and lipid. While water and lipid do have some absorbing properties, they absorb much less than blood. Another chromophore, met-haemoglobin (metHb) can, depending on the blood, be a significant absorber. Although blood is predominantly composed of different types of haemoglobin[3], it also contains other components such as plasma. The hematocrit value gives the fraction of Hb that makes up whole blood [17]. It is approximately calculated as $[\mathrm{Hb}] = \mathrm{B}\%\frac{150g/L}{370g/L}$ where B% is the concentration of whole blood in a sample[18].

A short introduction of the biological functions of HHb, HbO_2 and metHb is given here.

Hb is the main component of red blood cells. Its primary biological function is to facilitate the transportation of oxygen and carbon dioxide between the lungs and the rest of the body. This is done by HHb and HbO_2, the latter which has a high affinity for oxygen [19]. The oxygen saturation, SO_2, is a measure of the relative concentration of HbO_2 and is defined as:

$$\mathrm{SO}_2 = \frac{[\mathrm{HbO}_2]}{[\mathrm{HHb}] + [\mathrm{HbO}_2]}. \tag{2.5}$$

metHb is another type of haemoglobin molecule whose molecular state has been altered, thereby inhibiting its ability to bind with oxygen. metHb concentrations of a healthy human should not exceed 1% [20].

Absorption Coefficient: μ_a

The absorption coefficient describes the probability of a photon being absorbed per unit length. The probability, P, of a photon "surviving" a propagation distance of L is given by: $P = e^{-\mu_a L}$. Additionally, when light is transmitted through a purely absorbing medium, the decrease in the transmitted light intensity after propagating a distance L is described by

[1] Where h is Planck's constant ($6.63 \times 10^{-34} m^2 kg/s$), c is the speed of light, and λ is the wavelength of the light.

[2] consisting mainly of different types of haemoglobin including deoxygenated (HHb) and oxy-haemoglobin (HbO_2))

[3] Collectively referred to as Hb

Beer-Lambert's Law:

$$I = I_0 e^{(-\mu_a L)}, \tag{2.6}$$

where I_0 is the incoming intensity and I is the transmitted intensity.

The general formula for the absorption coefficient of a specific medium consisting of various chromophores is given by Equation 4.3a:

$$\mu_{\mathrm{a}}(\lambda) = \Sigma_{\mathrm{i}} \varepsilon_{\mathrm{i}}(\lambda) C_{\mathrm{i}}, \tag{2.7}$$

where ε_{i} is the extinction coefficient of a chromophore (wavelength dependent, units $\mathrm{cm}^{-1}\mathrm{M}^{-1}$) and C_{i} is the concentration of that chromophore. For blood, the molar mass of Hb is 64500 $^{g}/_{mol}$ and a typical concentration of Hb is 150 $^{g}/_{L}$ [21]. Using these values for the molar mass and concentration, the absorption coefficient of Hb is calculated by:

$$\mu_{a,Hb} = 2.303 \frac{150 \times \varepsilon_{Hb}}{64500}. \tag{2.8}$$

Equation 2.8 gives the absorption coefficient for a volume fraction of 100% Hb. In order to calculate the absorption coefficient of Hb for other volume percents, Equation 2.8 must be multiplied by 0.5 for 50% volume percent, 0.25 for 25% volume percent, etc[4].

For modelling the absorption coefficients of a tissue consisting of HHb, HbO_2, and water the above equation is rewritten as:

$$\mu_a(\lambda) = S_B((1 - SO_2)\mu_{a,HHb}(\lambda) + SO_2 \mu_{a,HbO_2}(\lambda)) + S_W \mu_{a,W}(\lambda). \tag{2.9}$$

The first two terms are the contributions of deoxygenated and oxygenated haemoglobin respectively, and the last term is the contribution of water on the absorption coefficient. The coefficients S_B and S_W are the blood and water fractions respectively while SO_2 is the oxygen saturation of the blood. Equation 2.9 can be expanded to account for other chromophores such as lipid, bile etc. by adding their respective terms (e.g. $S_{lipid}\mu_{a,lipid}(\lambda)$+$\mathrm{S}_{bile}\mu_{a,bile}(\lambda)$...).

The absorption spectra of HHb, HbO_2, metHb, water, and lipid are shown in Figure 2.2 [22].

[4]Concentrations throughout this thesis are referred to their volume percents.

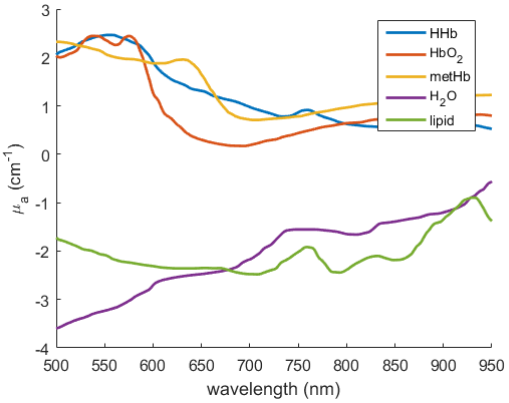

Fig. 2.2 Absorption coefficients of common chromophores plotted on a log scale. Each chromophore is plotted for 100% percent volumes.

2.2 Forward Models: Modelling light propagation in tissue

As discussed previously, the propagation of light in tissue is determined by absorption and scattering events. The probabilities of these events occurring, as well as the mfp of the photon between each interaction, and the isotropy of the light after being scattered are contained in two coefficients: μ_a, and μ_s'.

The Radiation Transport Equation (Equation 2.10) mathematically describes the propagation of light through a medium where the speed of light is v.

$$\frac{1}{v}\frac{\delta L}{\delta \mathrm{t}} + \hat{\Omega}\cdot\nabla L = -\mu_t L + Q(\mathbf{r},\hat{\Omega}',t) + \mu_s \int_{4\pi} L f(\hat{\Omega},\hat{\Omega}')d\Omega'. \tag{2.10}$$

Before discussing the above equation, some technical terms will be defined.

2.2.1 Vocabulary

Light Radiance

Light radiance, $L(r,\hat{\Omega},t)$, is defined as the light power per unit area travelling in a certain direction ($\hat{\Omega}$), at a certain position and time (r,t).

Photon Fluence Rate

The photon fluence rate, $\Phi(r,t)$, is the total light power per unit area leaving an infinitesimal volume at a position r and time t. In other words:

$$\Phi(r,t) = \int_{4\pi} L(r,\hat{\Omega},t)d\Omega. \tag{2.11}$$

Photon Flux

The Photon Flux, $\mathbf{J}(r,t)$, defines the total vector sum of light radiance leaving an infinitesimal volume with a direction $\hat{\Omega}$.

$$\mathbf{J}(\mathbf{r},t) = \int_{4\pi} L(\mathbf{r},\hat{\Omega},t)\hat{\Omega}d\Omega. \tag{2.12}$$

2.2.2 The Diffusion Equation (DE)

The right hand side of the RTE introduced previously (Equation 2.10) describes the loss of light radiance through absorption and scattering events[5], as well as the gain in radiance through scattering events which scatter the light from a certain direction $\hat{\Omega}$ to $\hat{\Omega}'$[6] and the gain in radiance by sources at a position r, at time t, emitting light in the direction $\hat{\Omega}$[7]. The left hand side is the time derivative of radiance in an infinitesimal volume element about r at a time t, travelling in a direction $\hat{\Omega}$ [23].

The solution to the RTE is non-trivial. Numerical solutions are obtained using certain approximations. One approximation gives a solution known as the Diffusion Equation (DE). The main aspects of the derivation of the DE is given here, however the complete derivation of the DE can be found in [23].

To simplify the solution of Equation 2.10, the radiance is expanded as spherical harmonics. Furthermore, by assuming an isotropic source, the spherical harmonics series is truncated to:

$$L(r,\hat{\Omega},t) = \frac{1}{4\pi}\Phi(r,t) + \frac{3}{4\pi}\mathbf{J}(r,t)\cdot\hat{\Omega}. \tag{2.13}$$

[5] $\mu_t = 1/(\mu_s + \mu_a)$
[6] $f(\hat{\Omega},\hat{\Omega}')$ is the probability of light travelling in a direction $\hat{\Omega}$ to be scattered into the direction $\hat{\Omega}'$
[7] $Q(\mathbf{r},\hat{\Omega}',t)$ is the power per unit volume emitted from position r at time t in a direction $\hat{\Omega}'$

Applying this approximated form of the radiance and integrating the Radiation Transport Equation over all solid angles, the time resolved Diffusion Equation is derived[8]:

$$D\nabla^2\Phi(\mathbf{r},t) - v\mu_a(\mathbf{r})\Phi(\mathbf{r},t) - \frac{\delta\Phi(\mathbf{r},t)}{\delta t} = -vS(\mathbf{r},t). \tag{2.14}$$

In the above equation, D(r) is the photon diffusion coefficient:

$$D(\mathbf{r}) = \frac{v}{3(\mu_s'(\mathbf{r}) + \mu_a(\mathbf{r}))}. \tag{2.15}$$

Solutions to the Diffusion Equation and photon fluence rate can in certain cases be given by various Green's functions depending on the geometry of the system. Farrell et al. present a method of solving the Diffusion equation for a semi-infinite geometry using dipole sources [24]. When making measurements, it is the reflectance, or the photon current leaving the tissue at the position z=0 that is of interest. The DE solution for the reflectance of a system with a semi-infinite geometry solved using image sources is given by [25]:

$$R[\mu_a(\lambda),\mu_s'(\lambda),\rho] = \frac{\mu_s'}{4\pi(\mu_s'+\mu_a)}\left[z_0\left(\mu_{eff}+\frac{1}{\widetilde{r_1}}\right)\frac{exp(-\mu_{eff}\widetilde{r_1})}{\widetilde{r_1}^2} + (z_0+2z_b)\left(\mu_{eff}+\frac{1}{\widetilde{r_2}}\right)\frac{exp(-\mu_{eff}\widetilde{r_2})}{\widetilde{r_2}^2}, \right. \tag{2.16}$$

where ρ is the source-detector separation, $\mu_{eff} = [3\mu_a(\mu_a+\mu_s')]^{1/2}$ is the effective coefficient, $z_0 = (\mu_a+\mu_s')^{-1}$ is the location of the image source, and $z_b = 2AD$, where D is the diffusion coefficient (Equation 2.15) and A is a parameter approximately equal to 1. The variables $\widetilde{r_1} = (z_0^2+\rho^2)^{1/2}$ and $\widetilde{r_2} = \left[(z_0+2z_b)^2+\rho^2\right]^{1/2}$ are the distances between a scattering/image source and the detection fiber respectively [25].

The validity of the Diffusion Equation and its solutions are limited to the approximations made in Equation 2.13, which are only valid if the source is nearly isotropic. Practically, this requires the medium to be highly scattering and also requires a SDS that is long relative to the photon's mean free length, $1/(\mu_s'+\mu_a)$.

2.2.3 The Monte Carlo Method (MC method)

The Diffusion Equation breaks down for highly absorbing tissues, as well as for systems with short source detector separations. In this regime, Monte Carlo (MC) methods are commonly

[8] $S(\mathbf{r},t)$, is the total power per volume emitted from position r, at a time t, i.e. $S(\mathbf{r},t) = \int_{4\pi} Q(\mathbf{r},\hat{\Omega},t)d\Omega$.

used for solving the Radiation Transport Equation. MC methods have also been proven to be useful when modelling complex tissue compositions [26]. Although several different Monte Carlo methods exist such as white, scaled, geometry-splitting methods, etc. [27–29], the Monte Carlo method used in this work is a modified version of the MCML method developed by Jaques et. al [30].

MC methods are stochastic methods that describe the transport of light in tissue based on the random sampling of variables. Consider a variable (such as step size), χ with a probability density function, $\rho(\chi)$, normalised to unity over the range $\chi(a,b)$ so that $\int_a^b \rho(\chi)\mathrm{d}\chi = 1$. In order to sample χ randomly, a random number (η) between 0 and 1 is generated. The probability density function of η is defined as $P(\eta)$. The cumulative distribution function of $P(\eta)$ is $F_\eta(\eta)$. There then exists a function $F_\chi(\chi)$ which can map the value of η to select the corresponding value of χ. In this way, random values for variables are chosen.

In a Monte-Carlo method, photon packages originate from a point source and travel a certain path length. Each photon package is assigned a weight equal to unity at the time of launch.

The path length of the photons, Δs, is updated with a probability $P = e^{-\mu_t \Delta s}$. The path length is reassigned at every step. After each step a fraction of the photon weight interacts with the tissue through an absorption event, and the remaining fraction in a scattering event. When the photon is scattered, the scattering angle is determined by the Henyey-Greenstein function. The photon position is updated accordingly.

With each such tissue interaction, the photon weight is updated to take a new value, $W = W - \Delta W$, and the updated weight is stored in the local grid element.

$$\Delta W = W \frac{\mu_a}{\mu_s + \mu_a}. \qquad (2.17)$$

After a photon package has experienced several absorption events, its weight will be substantially reduced. Propagating a photon

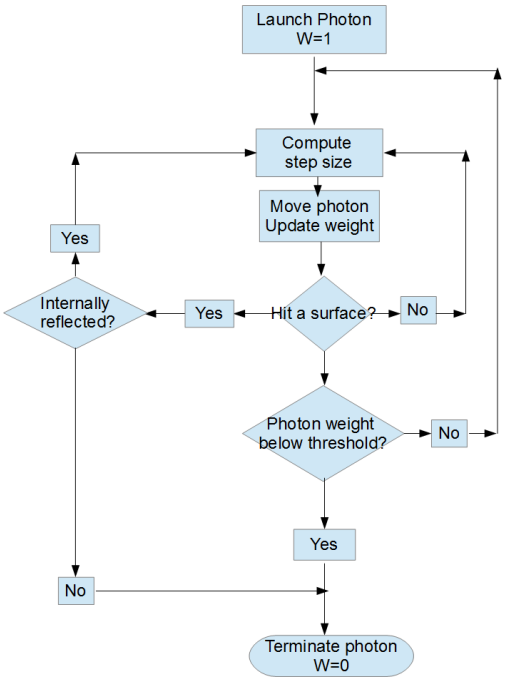

Fig. 2.3 Flow chart outlining the Monte Carlo method

package with a small weight gives little information, and therefore there must be a criterion for terminating photons. The photon package is terminated through 'roulette' where a photon package whose weight is below a certain threshold is given a certain probability to survive, otherwise the weight is reduced to zero and in this way terminated.

Monte Carlo look up tables are tabulated values of the reflectance for different μ_a and μ_s values calculated using the Monte Carlo forward model. These tables are commonly used when fitting parameters to experimental using the inverse model.

2.3 Inverse Problem: Determining chromophore concentrations

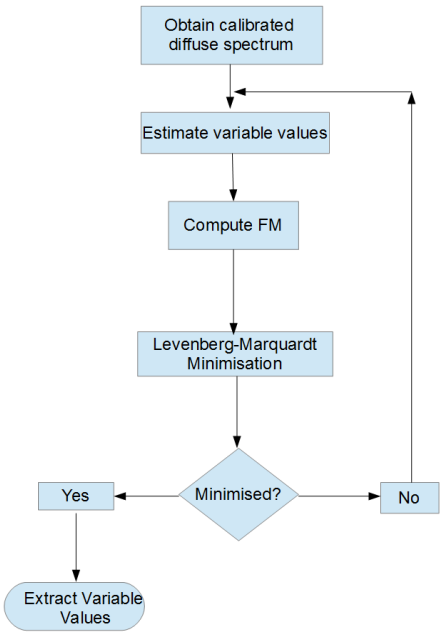

Fig. 2.4 Flow chart outlining the process of executing the Inverse Problem.

The inverse problem fits the FM with measured spectral data. The FM contains several variables such as chromophore concentrations required to calculate μ_a and scattering parameters. These variables must be calculated and updated to minimise the difference between the forward model and the spectral data. The minimisation algorithm used is known as the Levenberg-Marquardt algorithm, the details of which are outlined in the following section.

Figure 2.4 shows a flow chart for how the Inverse Problem is executed.

Levenberg-Marquardt Algorithm

The Levenberg-Marquardt Algorithm is a commonly used minimisation algorithm. It improves on other minimisation algorithms by considering both derivatives and second derivatives of the function being minimised.

In the context of this work, the Levenberg-Marquardt Algorithm is used to

minimise the difference between the experimental data, $y_e(\lambda)$, and the FM, $y_{FM}(\lambda;\mathbf{P})$, by updating the variable parameters, $\mathbf{P}$ of the FM,.

Considering a spectrum with a total of m data points, the total function to be minimised is:

$$\Omega(\mathbf{P}) = \sum_{i=1}^{m} [y_e(\lambda_i) - y_{FM}(\lambda_i;\mathbf{P})]^2. \tag{2.18}$$

In order to minimise the value of $\Omega(\mathbf{P})$, the Gradient Descent method offers a simple solution for updating P using the gradient, $\nabla\Omega(\mathbf{P})$. The update of P in this case is:

$$\mathbf{P}_{x+1} = \mathbf{P}_x - \eta\nabla\Omega, \tag{2.19}$$

where η is a parameter which determines the step-size.

A clear disadvantage of updating $\mathbf{P}$ in this way is if we consider a shallow minimum well. The stepsizes will be very small and it will take many updates to progress down to the minimum. Also, if we consider a steep well where the bottom is the minimum, we risk exiting the well when updating the parameters along the steep edges of the well.

The Gauss-Newton method is an alternative to the Gradient Descent method that is useful when $\Omega(\mathbf{P})$ is close to its minimum value. This method approximates $\nabla\Omega(\mathbf{P})$ to a quadratic function by substituting its second order Taylor expansion to Equation 2.19. The limitation of the Gauss-Newton method is it is only valid near the solution and is highly dependent on the initial values of $\mathbf{P}$.

The Levenberg-Marquardt method updates the parameters in the following way:

$$\mathbf{P}_{x+1} = \mathbf{P}_x - [\nabla^2\Omega(\mathbf{P}) + \eta\,\mathrm{diag}(\nabla^2\Omega(\mathbf{P}))]. \tag{2.20}$$

The Levenberg-Marquardt algorithm converges to the Gradient Descent method far away from the solution and to the Gauss-Newton method near the solution. Additionally, by using the diagonal matrix, the value of η is not as problem dependent as for the other minimisation methods [31].

There are many available numerical implementations of the Levenberg Marquardt algorithm. In this work, the lsqnonlin function provided in MATLAB has been used when computing the inverse model.

2.4 This Work

To conclude this chapter, a more detailed overview of the aims of this work and their relevance to the theoretical background given is provided:

2.4.1 Acquisition of Diffuse Reflectance Spectra

DRS was used to acquire the diffuse relectance spectra of light after propagating through a liquid phantom sample. These spectra were calibrated and the calibrated spectra used to solve the inverse problem using both the DE and a MC look-up table.

2.4.2 Acquisition of Transmission Measurements

Transmission measurements were made in order to determine the absorption coefficients of the main absorbers in the liquid phantoms, blood. Taking the transmission measurements was crucial for this work since the blood used for the phantom studies was ordinary bovine blood purchased from a grocery store. Therefore, the chromophore composition and hematocrit values of the blood used are not well-known. The relative intensities of light before and after being transmitted through a sample of blood and water solution were recorded. Using Beer-Lambert's Law (Equation 2.6), the values of $\mu_a(\lambda)$ were determined. These experimental values of μ_a were used when developing the evaluation protocol for solving the inverse problem.

2.4.3 Implemention of the Inverse Model

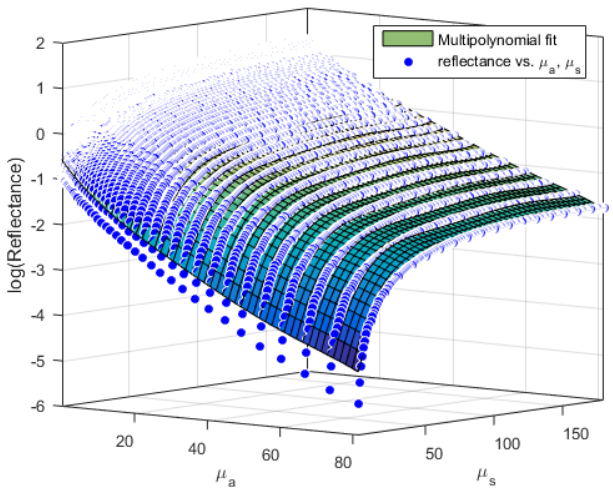

Fig. 2.5 A MC look-up table.

The inverse problem was solved to determine the chromophore compositions of tissue-mimicking liquid phantoms using both the Diffusion Equation and Monte Carlo methods. The values of μ_a obtained through the transmission measurements were used to calculate the forward model. Equation 2.16 is used to calculate the forward model spectra when implementing

the Diffusion Equation. However, when implementing Monte Carlo a Monte Carlo look-up table is used. An example of such a look-up table calculated for a pencil-beam photon package containing 10^8 photons in a tissue with an anisotropy factor g=0.7, and at a SDS of 0.5 mm is shown in Figure 2.5. The reflectance was simulated for μ_a values between 0 and 80 cm^{-1} and μ_s values between 0 and 180 cm^{-1} The resolution for both μ_a and μ_s when creating the look-up table is 1 cm^{-1}. A 5th degree (for both μ_a and μ_s axes) multipolynomial plane was fit to the simulated reflectance data points in order to be able to evaluate the reflectance for any value of μ_a and μ_s.

Chapter 3

Methods

3.1 Overview

The overall purpose of this work is to develop a suitable evaluation protocol of liquid phantom chromophore compositions using DRS. In order to develop such a protocol, the steps outlined in Section 1.3 were performed. In this chapter, the experimental methods for developing the evaluation protocol are given. First, the simulation methods for determining the light penetration depth in tissue will be outlined followed by the experimental setup for transmission measurements used to characterise the absorption properties of bovine blood. Then, the method for creating the liquid phantoms is discussed. Finally, the experimental setup for performing DRS measurements as well as various calibration techniques are introduced.

3.2 Light Propagation Simulations

Simulations were made in order in order to determine the penetration depth of light in tissue. These simulations give a comprehensive understanding of the capabilities of this DRS system.

In order to determine the penetration depth, light propagation in tissue was simulated using the MCML and CONV programs written by L. Wang and S. Jacques [30, 32]. MCML is an acronymyn for '**M**onte **C**arlo **M**ulti-**L**ayered', and is a commonly used program within the field of biophotonics. It simulates the propagation of an infinitely narrow beam of light through a turbid multi-layer and infinitely wide medium using Monte Carlo. The number of layers, the thickness of the layers and their respective values for μ_a, μ_s, g, and n are provided by the user.

The quantities simulated are the photon absorption, fluence, reflection, and transmission.

CONV is a complementary program of MCML. CONV convolves the simulation results of MCML to give the results for the propagation of a narrow beam.

3.3 Transmission Measurements for Determining μ_a

Transmission measurements are carried out to determine experimental values of absorption coefficients of the main absorber in the liquid phantoms, bovine blood. Having experimental values of μ_a of the blood used will be useful when developing the evaluation protocol. A setup for measuring the transmission spectrum of a sample (mixture of bovine blood and water) was designed, and Beer Lambert's Law was used to determine μ_a.

3.3.1 Transmission Measurements: Sample Preparation

The samples of bovine blood and water solution were prepared with blood concentrations of 10, 5, 2.5, 1.25, 0.625, 0.3125, and 0.15625% respectively. The samples were sonicated for approximately one minute in order to allow the blood to fully disperse in the water.

3.3.2 Transmission Measurements: Experimental Setup

A small optical setup consisting of lenses and apertures was designed for performing the transmission measurements. Light from an Ocean Optics halogen lamp (HL-2000-FHSA) was sent through an optical fiber. The light exiting the fiber was focused and collimated using a lens and an aperture. From there, the light passed through a small 1 cm x 1 cm cuvette containing the sample. After passing through the sample, the transmitted light was again focused into another optical fiber using an aperture and lens. This optical fiber was connected to an Ocean Optics spectrometer (USB4000).

The experimental setup for the transmission measurements is shown in Figure 4.3.

3.4 Liquid Phantom Preparations and Calibration

Throughout this work, liquid phantoms are used as a substitute for real biological tissue since their true compositions are known. These liquid phantoms are a mixture of bovine blood, Intralipid® 20%[1], and water. Thus the main absorbers of the liquid phantoms are the

[1] Intralipid® 20% is used throughout this work, and will henceforth be referred to as Intralipid® or abbreviated as IL.

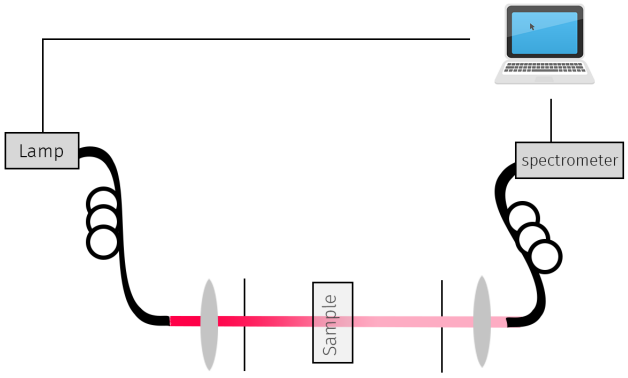

Fig. 3.1 Transmission measurement setup

constituents of the bovine blood used (HHb, HbO_2, metHb, etc.) and the main scatterer is IL. The liquid phantoms were made with varying volume fractions of absorber and scatter.

3.4.1 Phantom Preparation: Varying blood and lipid volume fractions

Phantoms consisting of 5, 7 and 10% IL were prepared. The concentration of the blood in the phantoms varied with different phantoms containing between 1 and 10% bovine blood. Water was then added to each sample so that the sum of the percent volumes of water, blood, and IL was 100%. The correct volumes of IL, blood, and water needed to create these phantoms were pipetted into glass vials. The phantoms were then sonicated for approximately one minute in order to properly disperse the solution.

3.5 Diffuse Reflectance Spectroscopy Instrument

A DRS setup is used to gather the data needed to evaluate the volume fractions of HHb, HbO_2, metHb, water and lipid of the phantoms as well as the Mie scattering parameters, a and b[2]. Additionally, for oxygenation studies, the accuracy to which the SO_2 value can be evaluated is tested using the same DRS setup. The diffuse reflectance spectra are acquired using two different probes with different source detector separations in order to determine the validity and limitations of the Diffusion Equation by fitting phantoms using both Diffusion Equation and a Monte Carlo method[3]

[2]Equation 2.3

[3]Evaluation of the liquid phantoms using Monte Carlo is done using a MC look-up table that was created by running MC simulations similar to MCML but modified to run on a graphics card [33].

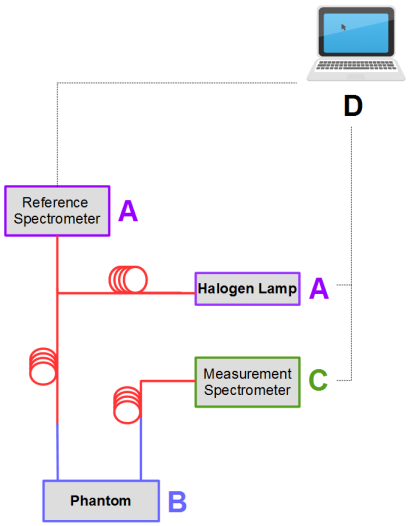

Fig. 3.2 DRS setup

The experimental setup is shown in Figure 3.2. The various components of the setup marked in Figure 3.2 will be discussed separately in the following sections.

3.5.1 A: Light Source and Reference Spectrometer

The Ocean Optics halogen light source is used for the DRS setup. In part A (purple) of Figure 3.2, the light source is connected to an optical fiber. The optical fiber is bifurcated so that some of the light from the halogen light is sent to a reference spectrometer and the rest is sent to be used in other parts of the setup. The reference spectrometer (Ocean Optics USB4000) therefore measures the spectrum of the light. The reference spectrometer is included in the setup so that any time dependent fluctuations of the lamp can be eventually corrected for.

The halogen light operates on TTL mode so that a measurement is taken at two times: one when the shutter is open, and another when the shutter is closed. Therefore, the reference spectrometer gathers two spectra per measurement. The first spectrum is the 'Data' spectrum i.e. the spectrum of the halogen lamp, and the other spectrum is the 'Background' spectrum i.e. the spectrum of any background light measured when the lamp shutter is closed. The two spectra will be referred to as R_{data} and R_{bkg} respectively.

3.5.2 B: Optical Probe and Liquid Phantom

The next portion of the setup labelled as 'B' (blue) in Figure 3.2 contains the liquid phantom and an optical probe. The preparation of the liquid phantoms was discussed in Section 3.4.1. Two different optical probes with source-detector separations[4] of 0.48 and 2 mm were used in this work. Sketches of the designs of these probes are shown Figure 3.3.

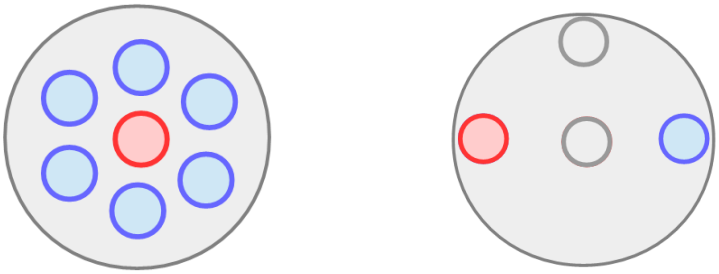

(a) *(b)*

Fig. 3.3 a: Probe design with 0.48 mm SDS b: Probe design with 2 mm SDS

The probes contain source and detector fibers coloured in red and blue respectively in Figure 3.3. The source fiber is connected to the halogen light source and delivers the light to the phantom. The light that is diffusely reflected from the sample is collected by the detector fiber(s) and sent to a spectrometer (section C of Figure 3.2). The optical probe with a SDS of 0.48 mm contains 6 detector fibers, however the other probe (SDS = 2 mm) uses only one detector fiber.

The phantoms studied using the 0.5 mm probe contained 5, 7, or 10% IL and 2, 4, 6, 8, or 10% bovine blood. The phantoms studied using the 2 mm probe contained 5, 7, or 10% IL and 1, 2, or 3% bovine blood. These main phantoms were used for calibration[5] and evaluation. In addition to these phantoms, another set of phantoms referred to as 'random' phantoms was prepared. These phantoms contained either 1, 3, 15, or 20% bovine blood and 3 or 20% IL. These 'random' phantoms were used in order to assess the robustness of the evaluation protocol.

3.5.3 C: Measurement Spectrometer

The diffusely reflected light is collected by the detector fiber and sent to the 'measurement' spectrometer. This spectrometer is similar to the 'reference' spectrometer and also collects

[4] SDS defined in Chapter 1
[5] See Section 3.6.3

'data' and 'background' spectra referred to as M_{data} and M_{bkg} respectively. The four spectra, R_{data}, R_{bkg} M_{data} and M_{bkg} are all used when calibrating the diffuse reflectance spectra. This will be discussed in more detail in Section 3.6.

3.5.4 D: Data Acquisition and Analysis

The entire setup is controlled via a computer, from which the exposure times as well as the number of measurements to be scanned to average can be input. The spectra are saved as .mat files, and all data analysis using these files is performed using MATLAB.

3.6 Calibration of Phantoms

The diffuse reflectance spectra (M_{data}) are initially calibrated using the reference spectrum from the lamp in order to account for any lamp fluctuations. These spectra are calibrated in the following way:

$$\text{Calibrated}_{\text{Lamp}} = \frac{M_{data} - M_{bkg}}{R_{data} - R_{bkg}} \times \frac{exp_R}{exp_M}, \tag{3.1}$$

where exp_M and exp_R are the exposure times for the measurement and reference spectrometers respectively.

After accounting for lamp fluctuations, other factors such as spectrometer and fiber responses etc., were calibrated using three different methods:

- Calibration using a Spectralon® puck. (Calibrates the two spectrometers and different optical fibers.)
- Calibration using an Intralipid®/Water phantom. (Calibrates the two spectrometers and different optical fibers.)
- Calibration using an Intralipid®/Water phantom and a Forward Model. (Calibrates the two spectrometers and different optical fibers, as well as the FM to the experimental data.)

These three calibration methods will be discussed below.

3.6.1 Calibration Method: Spectralon®

In the first calibration method, a Spectralon® puck was used to gather the spectrum of the halogen lamp lightsource. As mentioned in Chapter 1, Spectralon® is a perfect diffuse

surface and is therefore commonly used for such calibration methods. By acquiring a DR spectrum using the Spectralon®, both measurement and reference spectrometers measure the lamp spectrum. Therefore, this provides a method for calibrating the spectrometer and fiber responses of the measurement and reference spectrometers. The puck spectra (data and background) measured using the measurement and reference spectrometer are denoted by M_{data}^{Puck}, M_{bkg}^{Puck}, R_{data}^{Puck}, and R_{bkg}^{Puck} respectively. A calibration factor, ψ, is calculated using these spectra so that the total calibrated spectrum for the diffuse reflectance is:

$$\text{Calibrated}_{\text{final}} = \psi \times \text{Calibrated}_{\text{Lamp}}. \tag{3.2}$$

The calibration factor is defined as:

$$\psi = \frac{M_{data}^{Puck} - M_{bkg}^{Puck}}{R_{data}^{Puck} - R_{bkg}^{Puck}} \times \frac{\exp_R}{\exp_M}. \tag{3.3}$$

3.6.2 Calibration Method: Intralipid®

Although Spectralon® is a perfect diffuse reflector, it has a major drawback since the measured spectrum is very sensitive to the distance between the puck and the detector fiber. In order to rectify this problem, a water and IL solution was used in the same way as Spectralon® to calibrate the DRS measurements. The full expression for the calibrated spectrum calibrated in this way is also given by Equations 3.2 and 3.3.

3.6.3 Calibration Method: Liquid phantom and a Forward Model

A third calibration method was tested where in addition to calibrating the spectrum according to Equation 3.2 using Intralipid®, the diffuse reflectance spectrum was calibrated using a spectrum calculated using a forward model (DE or MC method) of a liquid phantom containing IL, whole blood, and water solution. The calibration factor, ψ, in this case is given by:

$$\psi = \frac{\text{FM}_{\text{phantomX}}}{\text{Exp}_{\text{phantomX}}}, \tag{3.4}$$

where $\text{FM}_{\text{phantomX}}$ is the forward model spectrum of a liquid phantom, phantomX, and $\text{Exp}_{\text{phantomX}}$ is the corresponding calibrated experimental spectrum of the same phantom. $\text{Exp}_{\text{phantomX}}$ is calculated by Equation 3.1.

Calibrating the diffuse reflectance spectra in this way not only calibrates the spectrum for lamp fluctuations, spectrometer and fiber responses etc., but also calibrates the spectrum to

the forward model method being used to solve the inverse problem. The full equation for calibrating the spectra is therefore given by:

$$\text{Calibrated}_{\text{Final}} = \frac{\text{FM}_{\text{phantomX}}}{\text{Exp}_{\text{phantomX}}} \left[\frac{\text{M}_{\text{data}} - \text{M}_{\text{bkg}}}{\text{R}_{\text{data}} - \text{R}_{\text{bkg}}} \times \frac{\text{exp}_{\text{R}}}{\text{exp}_{\text{M}}} \right]. \tag{3.5}$$

Chapter 4

Results and Discussion

The remaining two chapters will be dedicated to the experimental results and analysis of the DRS evaluation protocols developed for the two FMs. As outlined in Chapter 1, first the penetration depth of light in optically different materials are simulated to validate the scenarios for which the experimental set-up can be used. Secondly, calibration of the DRS spectra is discussed. Finally, the results of DE and MC forward models are presented and compared with each other as well as comparing the difference in results using probes with different SDSs. The spectral region considered for all parts of this work is between 500 and 900 nm.

4.1 Simulation of Probed Depth using MCML and CONV

The propagation of light through tissue was simulated using MCML and CONV programs in order to determine the depth that the light penetrated. Knowledge of the penetration depth gives some context to what this setup can be used for.

In order to simulate the transportation of light through a medium, two things must be known: the optical properties of the medium, and the basic properties of the light beam that is propagating through that medium. In order to simulate the optical properties of the medium, the absorption coefficients were calculated using the extinction coefficient values cited by Nachabe et.al. [22], and theoretical values for the reduced scattering coefficients of different concentrations of Intralipid® were calculated using the equation given in [34]:

$$\mu_s'(\lambda) = C(0.58\lambda - 0.1) \times 0.32\lambda^{-2.4}[\frac{\text{cm}^{-1}}{\text{mL/L}}], \tag{4.1}$$

where C is the concentration of IL in ml/L, and wavelength (λ) is given in μm.

The beam used in the simulations was modelled to be a Gaussian beam with an energy of 1J, and a 0.002 cm radius. Light of wavelengths 500, 540, 580, 620, and 660 nm was used in the simulations, and the penetration depths for probe setups with SDSs ranging between 0.5 to 4 cm were calculated.

4.1.1 One Layer Model

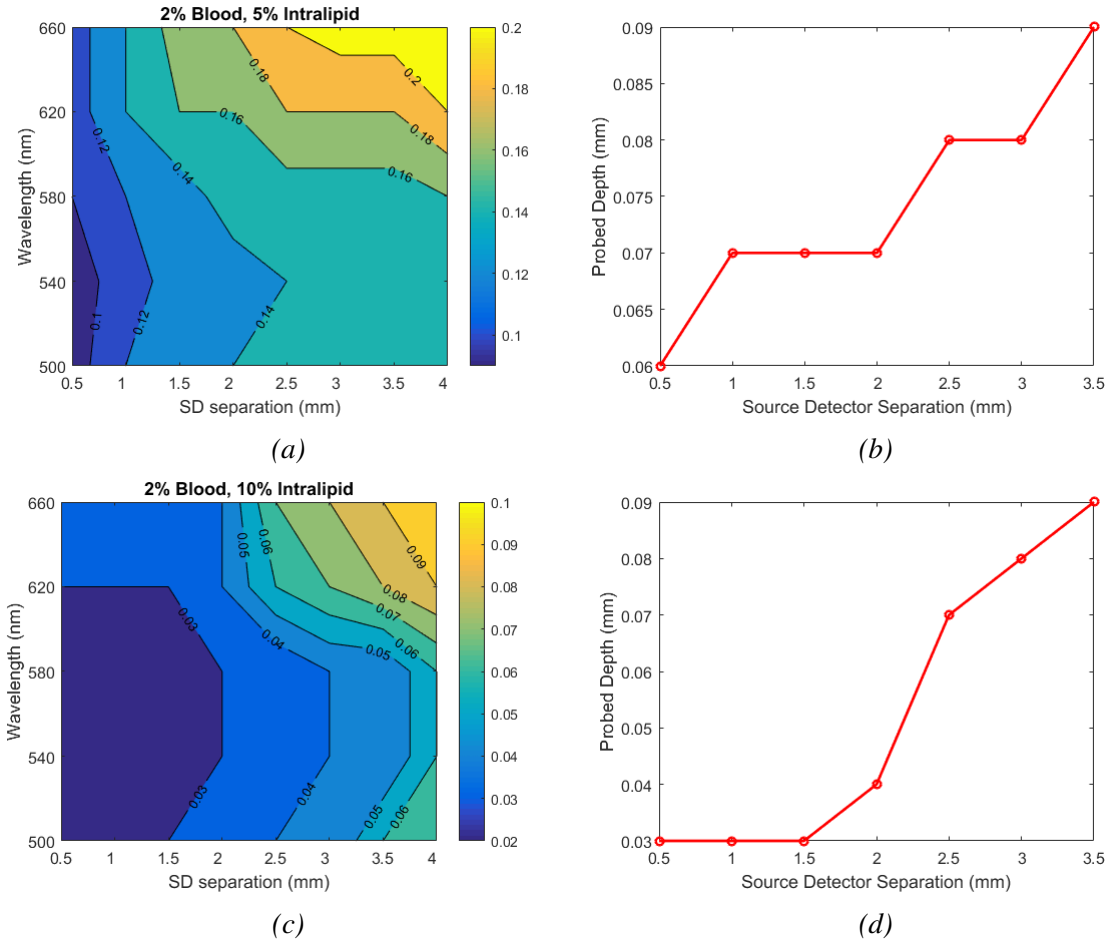

Fig. 4.1 Simulated penetration depths in millimetres for simulated media. a: Medium with 2% blood and 5% IL b: Probed depth as a function of SDS for medium in (a) measured at 660 nm. c: Medium with 2% blood and 10% IL d: Probed depth as a function of SDS for medium in (c), measured at 660 nm.

First, light transport through various homogeneous media with thicknesses of 100 cm consisting of various blood concentrations and lipid were simulated. In Figure 4.1, the simulated penetration depths for two of these simulated media are shown as functions of SDS and wavelength. The simulated media all had a constant SO_2 value of 74%, and a water

volume fraction of 95%. Also shown is the change in probed depth with SDS measured at 660 nm.

The results in Figure 4.1 generally indicate an increase in penetration depth with longer wavelengths and source detector separations. Shorter penetration depths at shorter wavelengths are expected since the absorption coefficient of blood is higher at shorter wavelengths (see Figure 4.3a below). Additionally, penetration depths are expected to be larger for longer source detector separations as derived by Weiss et.al [35].

4.1.2 Two Layer Model

A one layer homogeneous medium is of course an idealised model of a biological sample. To simulate a more realistic system, a two-layer model was simulated and the penetration depth of the light was calculated. The thickness of the top layer was set to 0.1 cm and the bottom layer had a thickness of 1 cm. The light beam had the same properties as before, and the penetration depths for the same wavelengths and SDSs were calculated.

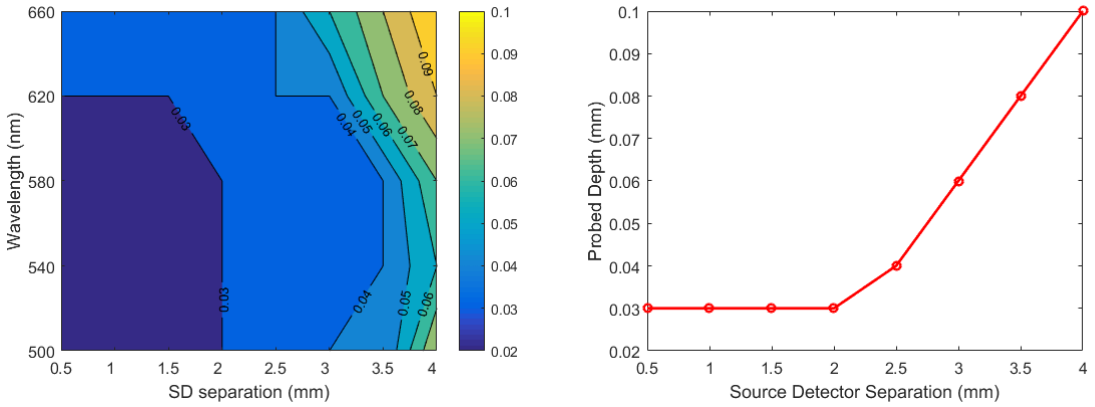

Fig. 4.2 a: Penetration depth as a function of SDS and wavelength. b: Penetration depth measured at 660 nm as a function of SDS.

For the two layer model simulation, the medium simulated has a top layer consisting of 10% lipid and 2% blood, while the bottom layer consists of 5% lipid and 2% blood. Both layers have water volume fractions of 95% and SO_2 values of 74%. Figure 4.2 plots the simulated penetration depths as functions of wavelength and SDS for the phantom.

Once again, the same dependence of penetration depth on wavelength and SDS is seen. The light again only penetrates a few μm, verifying that this setup for the probes used with SDSs of 0.5 and 2 mm can only be used to probe surface tissue.

4.2 Transmission Measurements

By recording the initial intensity, and the intensity of the light after having transmitted through a sample of blood, the absorption coefficients, μ_a, of the blood were determined. The calculated, smoothed values of μ_a for samples with varying concentrations of blood (10, 5, 2.5, 1.25, 0.625, 0.3125, and 0.15625%) are shown in Figure 4.3a. The variation of the absorption coefficient as a function of blood concentration at four different wavelengths is shown in Figure 4.3b. The clear linear fit with an intercept at zero shown in Figure 4.3b is indicative of accurate experimental results. Although the accuracy of the results is shown to be good, for high concentrations (10 and 5%) at low wavelengths, the signal is relatively noisy due to the high attenuation of the light and therefore these two concentrations will be discarded in further discussions.

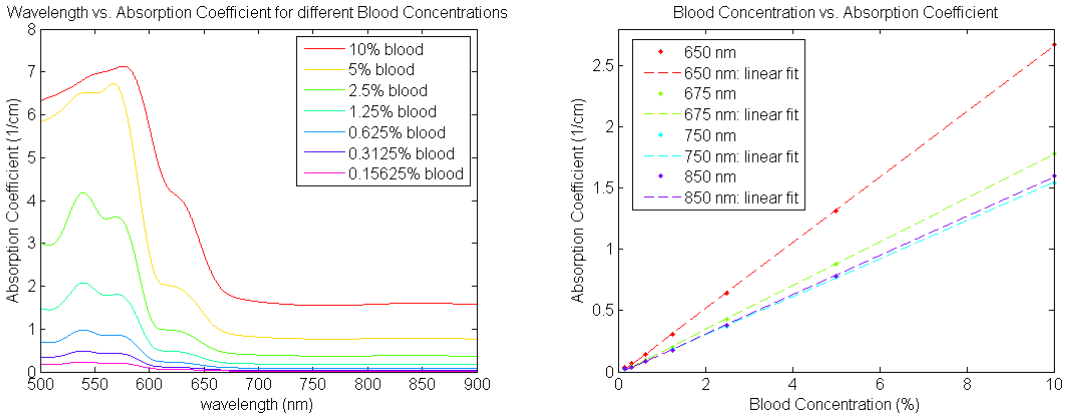

(a) *(b)*

Fig. 4.3 a: Calculated values of μ_a. b: linear fit of concentration and μ_a for four different wavelengths.

The concentrations of HHb, HbO_2, and metHb in the blood used were calculated via matrix division of the experimental values of μ_a (Figure 4.3a) and the extinction coefficients cited in [22]. Blood also contains some scattering properties and therefore this is also considered when fitting the absorption coefficients [36].

$$\begin{bmatrix} \mu_a^{\lambda_1} \\ \vdots \\ \mu_a^{\lambda_1} \end{bmatrix} = \begin{bmatrix} \varepsilon_{HHb}^{\lambda_1} & \varepsilon_{HbO_2}^{\lambda_1} & \varepsilon_{metHb}^{\lambda_1} & \varepsilon_{scatter}^{\lambda_1} \\ \vdots & \vdots & \vdots & \vdots \\ \varepsilon_{HHb}^{\lambda_N} & \varepsilon_{HbO_2}^{\lambda_N} & \varepsilon_{metHb}^{\lambda_N} & \varepsilon_{scatter}^{\lambda_N} \end{bmatrix} \times \begin{bmatrix} [HHb] \\ [HbO2] \\ [metHb] \\ [scatter] \end{bmatrix} \tag{4.2}$$

The resulting calculated values of μ_a of the transmission sample containing 0.15625% blood is plotted together with its corresponding experimental value in Figure 4.4a.

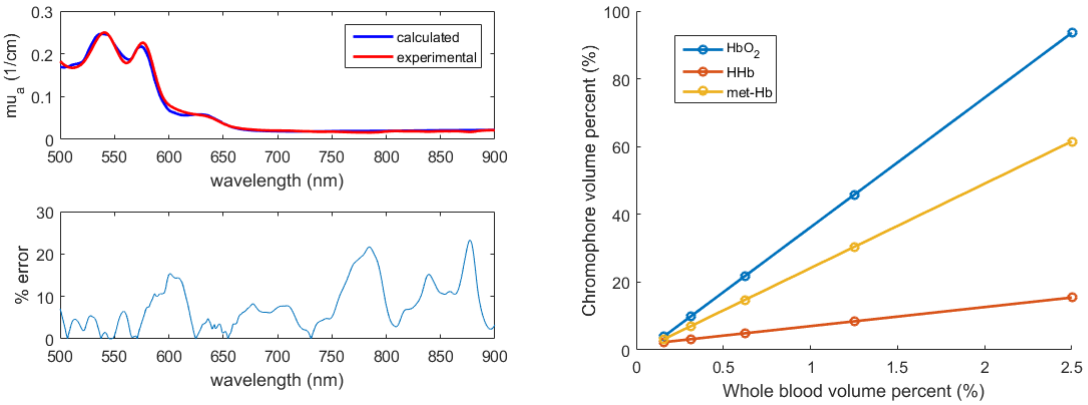

(a) *(b)*

Fig. 4.4 a: Experimental (red) and calculated (blue) values of mu_a. Percent error is also shown. b: Linear fit of chromophore concentrations to whole blood concentration.

Fitting all of the experimental data for the different blood transmission samples in the following way, the relationship between concentrations of HHb, HbO_2 and metHb as a function of volume percent of blood was determined. These linear relationships are shown in Figure 4.4b. These linear fits are considered to give the true values of chromophore concentration as a function of volume percent of whole blood and are used when determining the chromophore compositions of the liquid phantoms (Section 4.4 and 4.5).

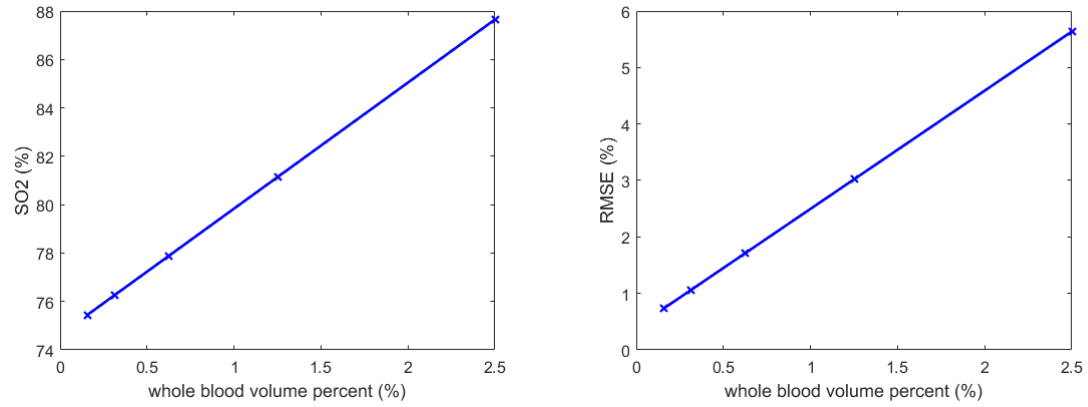

(a) *(b)*

Fig. 4.5 a: Linear fit of SO_2. b: RMSE of fits.

Finally, from the concentrations of HHb and HbO_2 shown in Figure 4.4b, the dissolved oxygen concentrations (SO_2) were calculated. This result is shown in Figure 4.5a. The figure shows a clear linear increase in the value of SO_2 with increasing blood concentration. Since SO_2 is only a relative ratio of the concentration of HHb and HbO_2, such a linear increase is unexpected. This can be explained by the presence of other chromophores such as myoglobin

(Mb) and oxy-myogolobin (MbO_2) which could affect the measured amount of SO_2. This hypothesis is supported in Figure 4.5b which shows the root mean square error (RMSE) of the experimental and fit values of μ_a for all transmission measurement samples. Figure 4.5b also shows a linearly increasing relationship between the RMSE value and concentration of whole blood.

4.3 Calibration Methods

In this work, a setup with two spectrometers was used. Therefore, calibration methods were developed that accounted for the differences in the responses of the spectrometers and fibers. The first two calibration methods deal solely with these system responses while the third is a calibration method that calibrates both the system responses and the FM to the experimental data using one calibration factor. The results of these calibration methods are discussed in the following sections.

4.3.1 Spectralon Puck

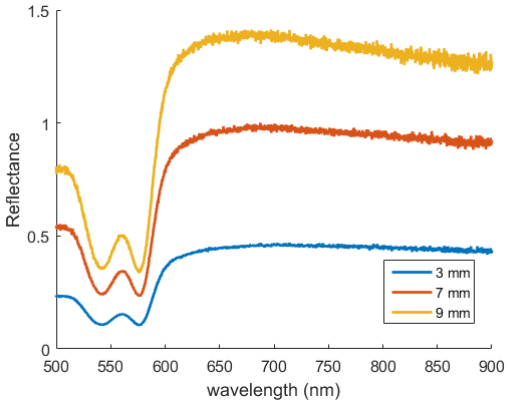

Fig. 4.6 Dependence of probe height on final calibrated spectra.

The first calibration method tested involved gathering the diffuse reflectance spectrum of a reflectance standard (Spectralon® puck). By measuring the reflectance spectrum of the puck, the two spectrometers (reference and measurement) can be calibrated to each other. Since the puck is a solid material, the probes were held at varying heights above the puck when taking the DRS measurements. The height at which the probe was held plays a large role in the final calibrated spectra. This is illustrated in Figure 4.6, where the spectrum of a

liquid phantom containing 7% IL and 4% blood is calibrated with the reflectance spectra of the Spectralon® puck taken at different heights.

4.3.2 Intralipid®

In order to eliminate the height dependence of the calibration using the reflectance puck, liquid solutions of IL and water are also used for calibration. The results of how the concentration of IL affect the final calibrated spectra are shown in Figure 4.7

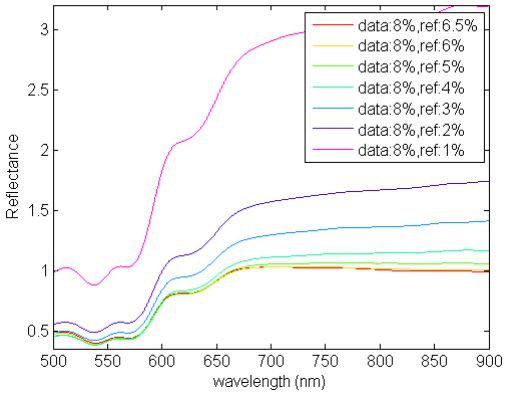

Fig. 4.7 Calibration using Intralipid®. The phantom being calibrated (data) contains 8% IL and the calibration phantoms contain varying amounts of IL (ref)

Although using a liquid as a reflectance standard eliminates the previous height dependency, Figure 4.7 indicates that when calibrating using a liquid solution of Intralipid® the concentration of scatterer is significant. Additionally, Intralipid® scatters light of shorter wavelengths more than light of higher wavelengths, meaning that Intralipid® cannot be used as a true reflectance standard and is only valid when the concentration of lipid in the phantom sample is similar to the concentration of lipid in the calibration sample. Obviously, this severely limits the applications in which IL solution can be used in calibrating DRS spectra. In order to overcome the limitations in the calibration methods using the Spectralon® puck and IL solution, a third calibration method using a forward model was developed.

4.3.3 Forward Model

The final calibration method tested involved calculating calibration factors for each of the diffuse reflectance spectra of the liquid phantoms[1] and their respective FM spectra.

[1] 15 for the probe with an SDS of 0.5 mm and 9 for the probe with an SDS of 2 mm.

These calibration factors are calculated by taking the ratio of experimental spectra and their respective FM spectra (Equation 3.4). The calibration factors account for the wavelength sensitivity between the DRS and FM spectra. Also, the difference in system response between the two spectrometers is contained in the calibration factor thereby eliminating the need of using a reflectance standard. To calculate the FM, μ_a was calculated using the values of μ_a of Section 4.2 extrapolated to 100% and μ_s was determined using Equation 4.1. The calibration factors for liquid phantoms with varying blood concentrations and a constant concentration of IL (7%) are shown in Figure 4.8a. These calibration factors are calculated using a MC forward model.

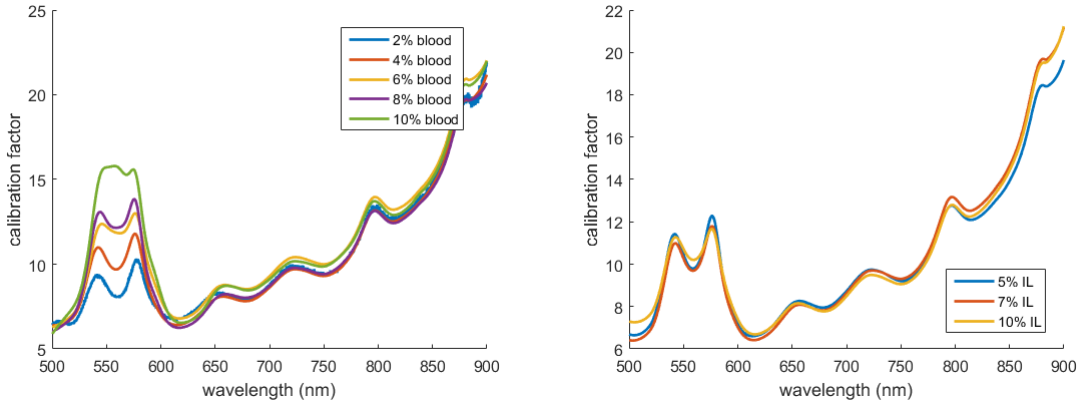

(a) *(b)*

Fig. 4.8 Calibration Factors. a: identical scatterer concentrations, different blood concentrations. b: identical blood concentrations, different scatterer concentrations.

In Figure 4.8b, the calibration factors calculated using MC from phantoms containing equal blood volume fractions and varying IL volume fractions of 5, 7, or 10% are shown. Comparing Figures 4.8a and 4.8b shows that although phantoms of different scatterer concentrations (Figure 4.8b) scale similarly to the forward model, varying blood concentrations scale very differently (Figure 4.8a). This blood concentration variation of the calibration factor is an unexpected and unwanted feature. Ideally, one would expect that so long as the FM has been calculated accurately using correct values of μ_a and μ_s, the ratio between the FM and experimental data would be the same for any phantom. The varying calibration factors can either be due to inaccurate values of μ_a or μ_s, an incorrect forward model, or something else entirely. In our case, μ_s is calculated using Equation 4.1, a well-cited value which is assumed to be true, and the experimental values of μ_a were verified to be accurate (Figure 4.3b). Assuming, with good reason, that the theoretical optical properties of the phantoms are accurately known, the discrepancies in the calibration factors can be attributed to a bad FM or something else. The forward model uses a MC look-up table calculated

using MCML which is a widely accepted program. Possible other sources of error can be inaccurate SDSs, as well as effects of the source beam. These two sources of error will now be considered.

SDS influences

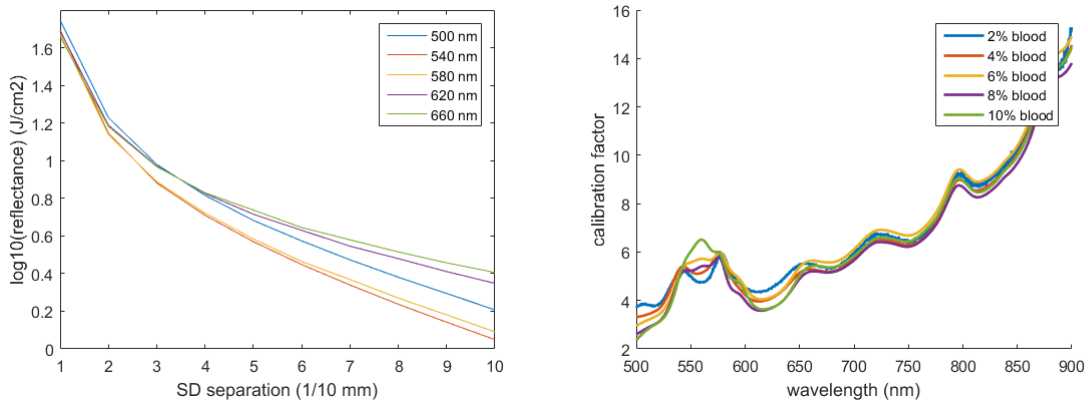

(a) *(b)*

Fig. 4.9 Changes in DRS with SDS. a: Simulation of how reflectance changes with SDS. b: Calibration factors measured when using a look-up table with an SDS of 0.7 mm. Experimental probe is cited to have an SDS = 0.48 mm.

The SDS quoted by the manufacturer is 0.48 mm. However, the MC look-up table only has a resolution of 0.1 mm. Therefore, the SDS of the short probe is estimated to be 0.5 mm. The longer probe was manufactured in house with an estimated SDS of 2 mm. However, the exact precision of the SDSs of these probes is not known. If the SDS is not accurate, this can result in inaccuracies in interpreting the MC look-up table and therefore result in discrepancies in the calibration factors as seen in Figure 4.8. Figure 4.9a is an MCML simulation showing the reflectance (log scale) as a function of SDS at 5 different wavelengths[2]. This simulation gives an idea of how the SDS affects simulated reflectance values.

Figure 4.9b shows how the calibration factors change when using a look-up table that was simulated at a SDS of 0.7 mm. This result suggests that perhaps the SDS of the probe is inaccurately evaluated. However, it is likely that the discrepancies in the calibration factors with blood concentration is due to a mixture of both inaccurate SDS as well as source beam influences. The latter effect will now be discussed.

[2]simulated phantom contains: 5% Intralipid® and 2% blood

Source beam influences

The original Monte Carlo look-up table was created by simulating a pencil beam of photons. This can lead to errors, especially at short SDSs. Therefore, it is possible that in order for the calibration factors of Figure 4.8a and 4.8b to be uniform, the look-up table must be convolved with the source beam. This would be prohibitively time-consuming to do using CONV for the look-up table used. In future work this will therefore be executed in a MATLAB script developed in house.

4.4 DRS using a probe with SDS=0.5 mm

As discussed previously, the calibration factors calcualted using MC differ depending on the concentration of blood in the liquid phantom. This is an error, and some suggestions on how to fix this have been discussed. However, here the results found using the average of all of the calibration factors[3] are shown. The results presented here will give an idea of how much the discrepancy in the calibration factors affect the final results. When using this probe, phantoms were made containing either 5, 7, or 10% IL and 2, 4, 6, 8, or 10% bovine blood.

4.4.1 Monte Carlo

The spectra obtained from the 15 liquid phantoms were used to calculate their corresponding calibration factors. The final calibration factor used for calibration is the average of all of these 15 calibration factors.

First, the Monte Carlo inverse problem was implemented to fit B% (whole blood concentration), a and b (Mie scattering parameters, Equation 2.3[4]). In this case, the absorption coefficient is defined as:

$$\mu_a = \mu_{a,measured} \times B\% \tag{4.3}$$

Where $\mu_{a,measured}$ is the average of the experimentally obtained values of μ_a in Section 4.2 extrapolated to 100% blood concentration. μ_s is defined by the equation for Mie scattering (Equation 2.3).

The results are shown in Figure 4.10. An example of an experimental spectrum[5] and a fitted spectrum[6] along with the percent error between the two spectra is shown in Figure

[3]Calibration factors evaluated for 15 phantoms, some of which were shown in Figure 4.8
[4]The phantoms are assumed to predominantly be Mie scatterers in the wavelength range used.
[5]labelled DRS
[6]labelled fitted

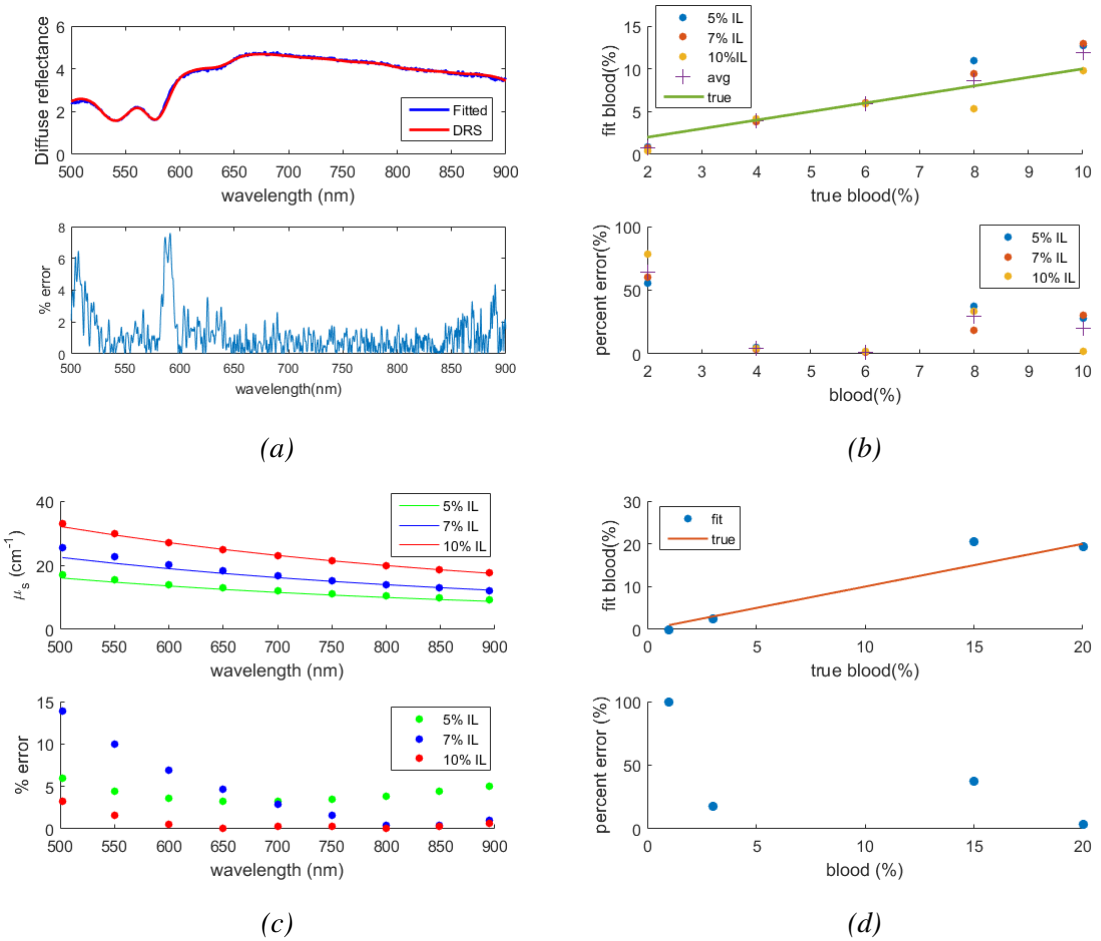

Fig. 4.10 Final results using MC and fitting for whole blood percent. a) DRS spectrum and fitted spectrum of a phantom containing 6% blood and 5% IL. b) Fitted and true values of B% along with their respective percent errors. c) Fitted and true values of μ_s at certain wavelengths along with their respective percent errors. d) Fitted and true values of B% for 'random' phantom set.

4.10a. The phantom contains 5% IL and 6% blood. The extracted values of whole blood concentration (B%) for the 15 liquid phantoms are shown in a scatter plot in Figure 4.10b plotted along with their true values. Figure 4.10c plots the average μ_s values at specific wavelengths along with their true values (solid line) and percent error of the fit.

The fitted values of B% and μ_s are very close to their expected values. The percent error for low blood concentration (2%) is high, over 50%, but excluding this data point B% is evaluated with an average percent error of 13.83% (Figure 4.10b). μ_s is also evaluated accurately with the percent error never exceeding 15% for any data point (Figure4.10c).

In order for this fitting and calibration procedure to truly be considered robust, liquid phantoms with optical properties outside of the range of optical properties of the phantoms used for determining the calibration factors should also be tested. The results of testing these

'random' phantoms is shown in Figure 4.10d. It is seen that the percent error of the fit value of B% is much less for higher blood concentrations (15 and 20%). These inaccurate evaluations of B% for low blood concentrations for both the phantoms used for calibration and in the 'random' phantom set indicate that the difference in calibration factor with different blood volumes is an issue that requires further attention.

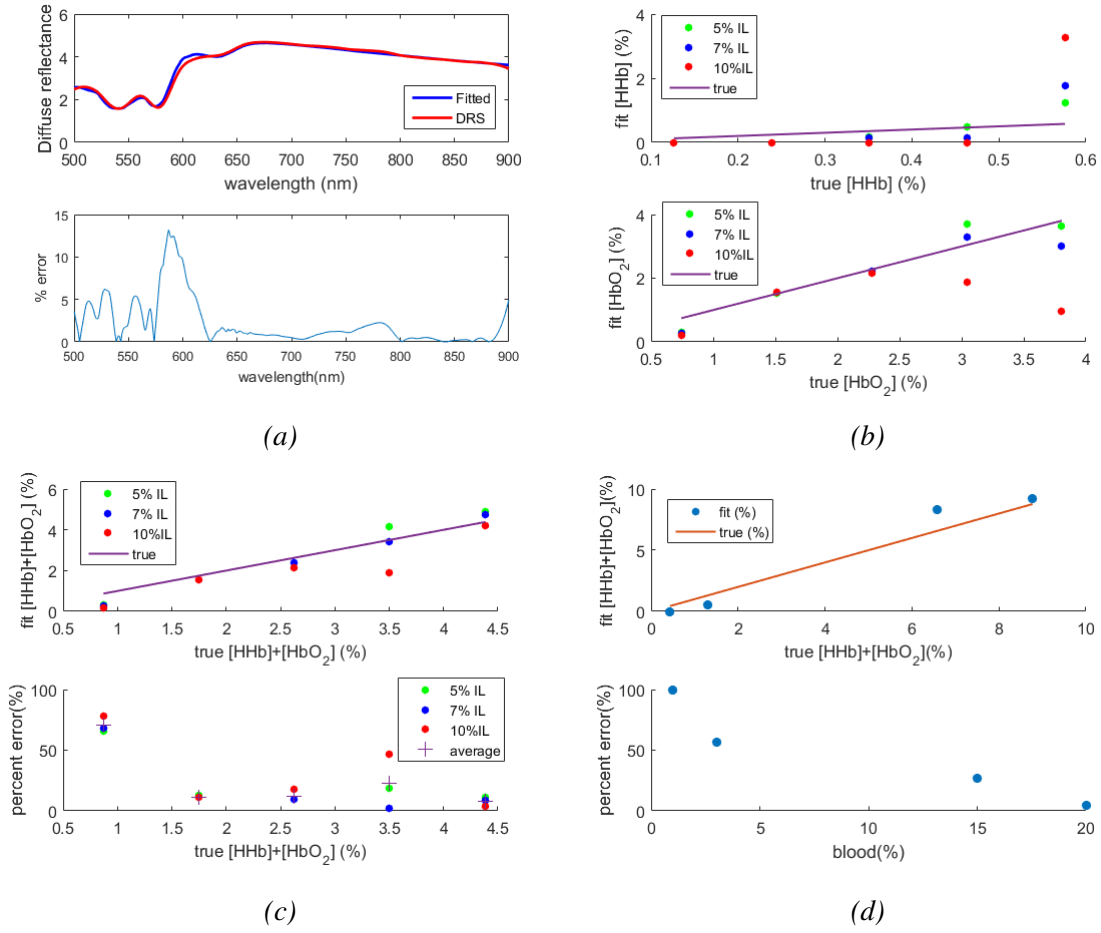

Fig. 4.11 Final results using MC and fitting individual chromophores. a) DRS spectrum and fitted spectrum of a phantom containing 6% blood and 5% IL. b) Fitted and true values of [HHb] and [HbO_2]. c) Fitted and true values of [HHb]+[HbO_2] along with their respective percent errors. d) Fitted and true values of [HHb]+[HbO_2] for 'random' phantom set.

Despite the fact that the calibration factors are not equal, it is still possible to fit the absorption and scattering parameters relatively well when considering whole blood. Now, the same method will be used to fit individual chromophores concentrations. In this case, the

absorption coefficient is given by[7]:

$$\mu_a = \varepsilon_{Hb} \times [Hb] + \varepsilon_{HbO_2} \times [HbO_2] + \varepsilon_{metHb} \times [metHb] + \varepsilon_{H_2O} \times 0.95 \tag{4.4}$$

The results obtained when fitting for individual chromophores is shown in the figures of Figure 4.11. Figure 4.11a shows the experimental and fitted spectra along with the percent error of the fit. In Figure 4.11b the fitted values of HHb and HbO_2 concentrations are plotted with their true values, while in Figure 4.11c the sum [HHb]+[HbO_2] is shown. Finally, Figure 4.11d shows the sum of [HHb] and [HbO_2] fit for the 'random' phantoms. The overall percent

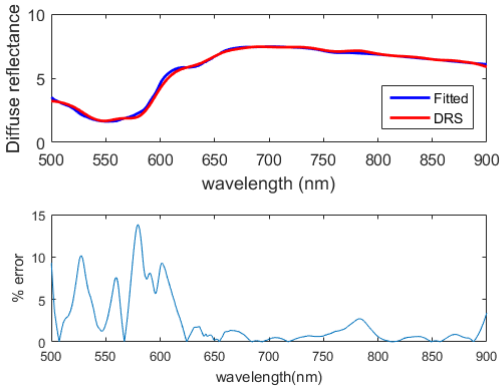

Fig. 4.12 DRS spectrum and fitted spectrum of a phantom containing 10% blood and 10% IL.

error of the fit of the DRS spectrum (Figure 4.11a) is worse when fitting with individual chromophores. This is expected since fitting μ_a with these parameters did not give a perfect fit. Although the sum of the fitted values [HHb]+[HbO_2] corresponds well with its true value for higher blood concentrations, the individual components [HHb] and [HbO_2] do not fit as well. This is especially true when evaluating phantoms with high blood concentrations. The good fit for [HHb]+[HbO_2] and bad fits for the individual components is understood by Figure 4.12 which shows the calibrated and fitted spectra of a phantom containing 10% IL and 10% blood. Clearly, the experimental spectrum no longer contains the characteristic absorption peaks of HbO_2 between 500 and 600 nm[8]. At these high blood concentrations, the signal is attenuated more strongly. This means the calibrated spectrum then looses its distinct characteristics making fitting of individual chromophores impossible.

[7]Note: Water concentration is fixed to 95% since its absorption is almost negligible in the wavelength region 500-900 nm. Additionally, lipid is shown to have negligible absorption properties compared to water in this wavelength region [37].

[8]See Figure 2.2.

Finally, the 'random' and experimental phantoms both show that the value of [HHb]+[HbO_2] is evaluated worse for phantoms with low blood concentrations. This trend was also seen previously when fitting for B%

4.4.2 Diffusion Equation

The calibration factors computed using the Diffusion Equation are shown in the following figure:

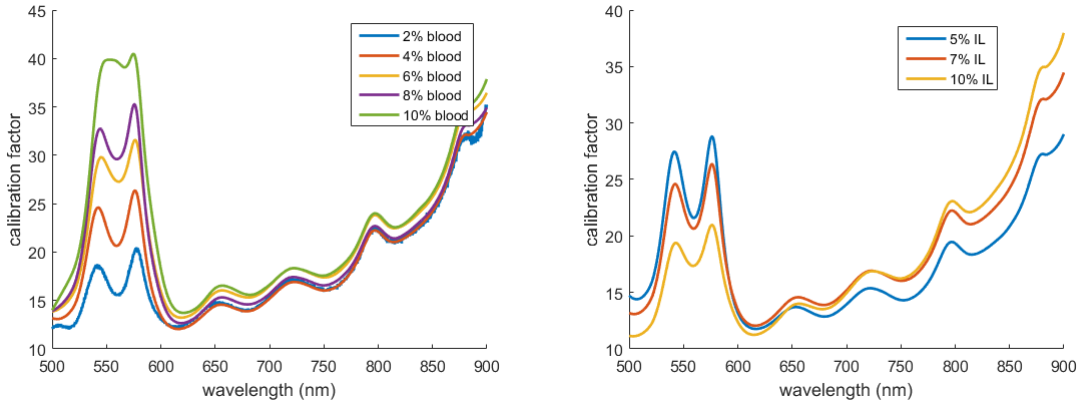

(a) *(b)*

Fig. 4.13 Calibration factors calculated using a DE FM. a: same IL concentrations, different blood concentrations. b: same blood concentrations, different IL concentrations.

The figures of Figure 4.13 show how the calibration factors calculated using DE change depending on blood and IL concentrations. The calibration factors calculated using MC were also dependent on blood concentration, however were independent of IL concentration (Figure 4.8b). Additionally, the blood concentration dependence of the calibration factors calculated using the DE is much larger compared to when using the MC forward model. Comparing the ratios between the calibration factors calculated using MC and DE models for phantoms with 10 and 2% blood at 557 nm, it was found that the discrepancy in calibration factors due to blood concentrations calculated using the DE differed 1.3 times more than when using MC. Therefore, the calibration factors themselves suggest the DE will yield less accurate results compared to MC. The average of all of the calibration factors was used when calibrating the spectra for evaluation using the inverse model.

Figure 4.14 shows the results obtained when using the DE to fit B% (Equation 4.3) and μ_s to the experimental spectra of both the phantoms used for calibration and the 'random' phantoms.

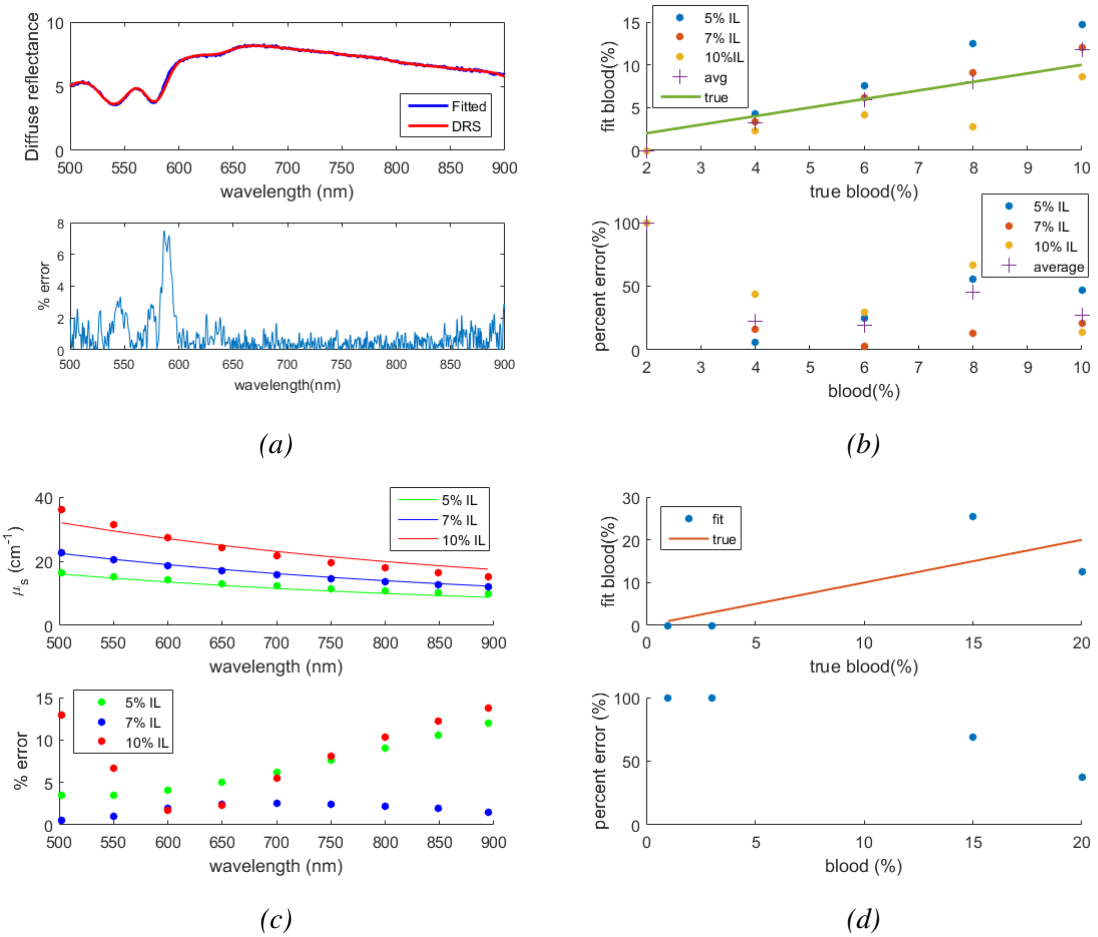

Fig. 4.14 Final results using MC and fitting individual chromophores. a: Fitting of phantom with 6% blood and 5% IL. b: Fitting of whole blood concentration. c: Fitting of μ_s at select wavelengths. True values shown as solid line. d: Fitting of whole blood concentration for random samples.

Although the percent error of the fit and experimental spectra is low (less than 8%), and comparable to the error in the fit using a MC forward model (Figure 4.10a), the fits for B% and μ_s are worse when evaluated using the DE. The average percent error for B%[9] evaluated using MC is 13.83% and when evaluated using DE this percent error is 28.33%. Comparing the fits of μ_s evaluated using MC and DE forward models (Figures 4.10c and 4.14c), the total average percent error of all data points using MC is 3.18% while using DE this error increases to 5.61%. Finally, the average percent error of the fits[10] for B% in the 'random' phantoms increases from 19.34% using MC to 68.84% using DE.

From these results, we conclude that as expected for short SDSs, using a MC forward model gives much more accurate results than using the DE.

[9] excluding the data point evaluated at 2% blood
[10] excluding the data point for 0.3% blood

4.5 DRS using a probe with SDS = 2 mm

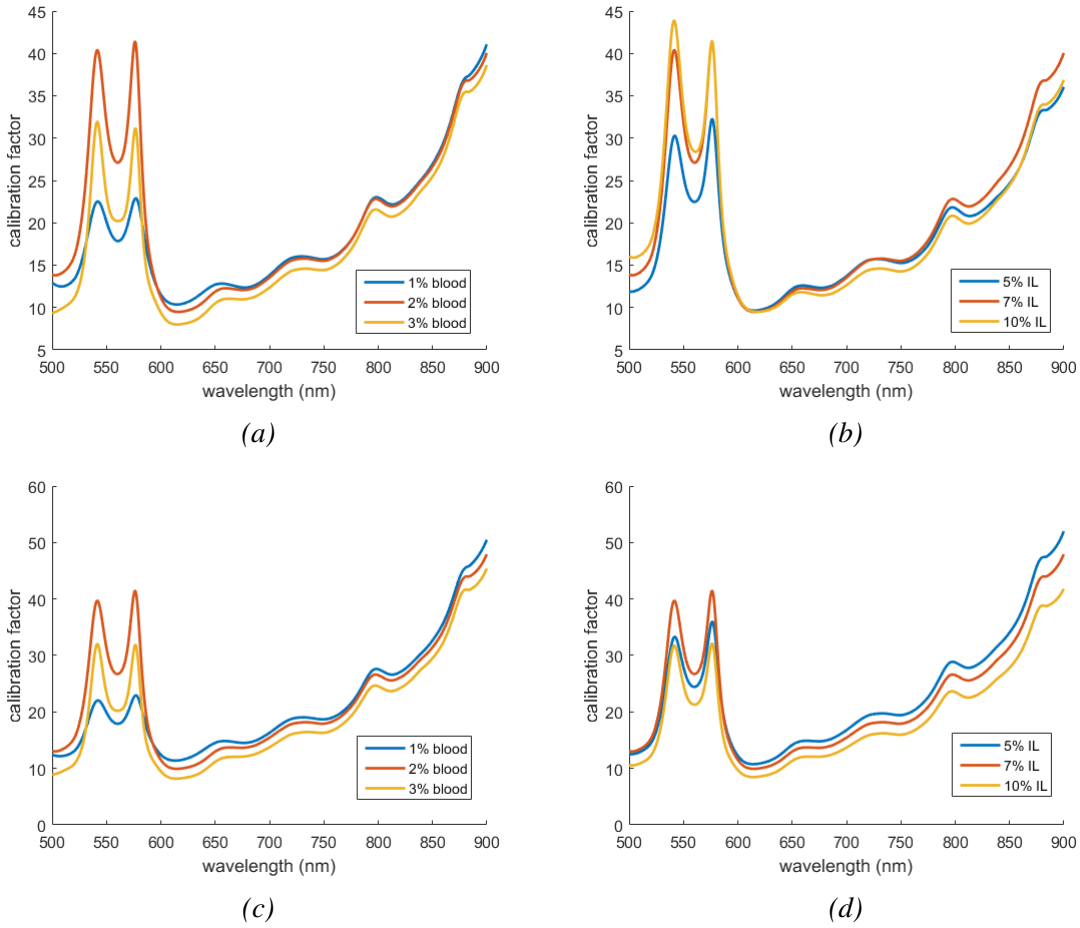

Fig. 4.15 Calibration factors calculated using a MC and DE FMs. a: same IL concentrations, different blood concentrations (MC). b: same blood concentrations, different IL concentrations (MC). c: same IL concentrations, different blood concentrations (DE). d: same blood concentrations, different IL concentrations (DE).

Diffuse reflectance spectra of phantoms containing 1,2, or 3% blood and 5, 7, or 10% IL were also measured using the probe with a 2mm SDS. Before discussing the results, the calibration factors calculated using these measurements (Figure 4.15) are discussed.

Once again, discrepancies in the calibration factors are seen when using phantoms with different blood concentrations for both MC and DE calibration factors. Possible sources of these discrepancies have already been discussed. Not seen previously for the MC calibration factors using the 0.5 mm probe are the discrepancies in calibration factors with different IL concentrations (Figure 4.15b). These new discrepancies can be a result of a worse planar

fitting to the MC look-up table for long SDSs[11]. Comparing the calibration factors calculated using the DE for phantoms with equal blood concentrations and different IL concentrations for the short SDS probe (Figure 4.13b) and the long SDS probe (Figure 4.15d), it is seen that the discrepancies between the factors is less using the long SDS probe.

4.5.1 Monte Carlo

The Monte Carlo method was used to determine the whole blood concentration (B%) of the liquid phantoms. These results are shown in Figure 4.16.

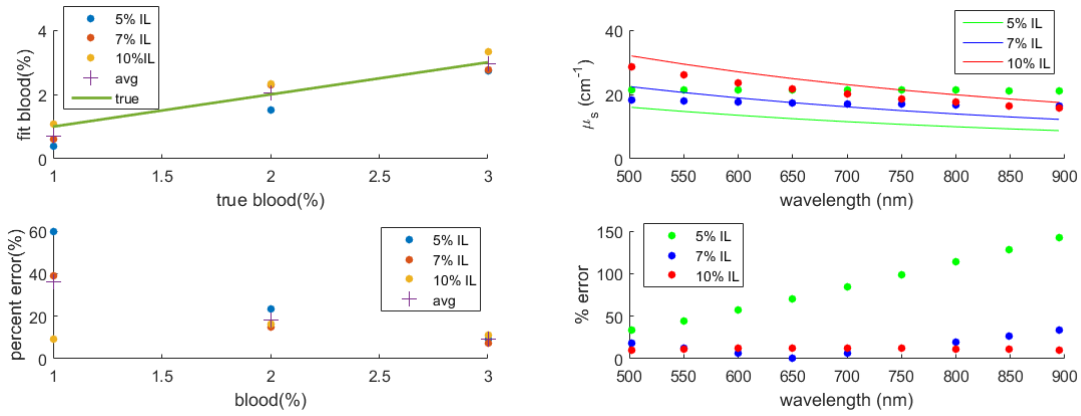

(a) *(b)*

Fig. 4.16 Results using MC for a probe with a SDS=2 mm. a) fitted values of whole blood concentration. b) μ_s fits and errors.

The results of Figure 4.16 show decent fittings for B% and μ_s. Phantoms with a low concentration of IL evaluated μ_s poorly, with the percent error at longer wavelengths exceeding 100%. μ_s is not expected to fit as well for this SDS since the calibration factors showed a discrepancy dependent on the IL concentration of the phantom. As mentioned previously, these results might improve by improving the planar fitting procedure of the MC look-up table.

It is not possible to directly compare the results of the long SDS probe to the short SDS probe since the phantoms used to evaluate the calibration factors contain different blood and IL concentrations and this affects the discrepancy of the calibration factors. On average however, the percent error of the average fitted values of B% are slightly lower when using the long SDS probe (21.2%) compared to the short SDS probe (23.96%). Additionally, the

[11] See Chapter 2.

average standard deviation of the percent errors for fitted B% values is slightly higher using the long SDS probe (8.7) compared to the short SDS probe (6.4).

These results (larger standard deviation but lower percent error using the longer probe) is unexpected when one considers the following:

- Convolution: As previously stated, convolution of the simulated source beam could affect the accuracy of the MC look-up table. At short SDSs, this influence would be more influential since the detected light has propagated a shorter distance and will be less diffuse. This hypothesis is verified from the result that the average percent error of the fitted value of B% is less when measuring the reflectance using a probe with a longer SDS.

- Calibration Factors: Comparing the calibration factors calculated using MC for the short and long SDS probes (Figures 4.8 and 4.15), it was observed that using the short SDS probe the calibration factors were independent of the concentration of IL, but they were dependent on the concentration of IL when using the other probe. This explains the larger standard deviation from the average value of the percent error of B% when using the probe with a 2 mm SDS. The origin for this is likely due to worse planar fitting of the MC look-up table.

4.5.2 Diffusion Equation

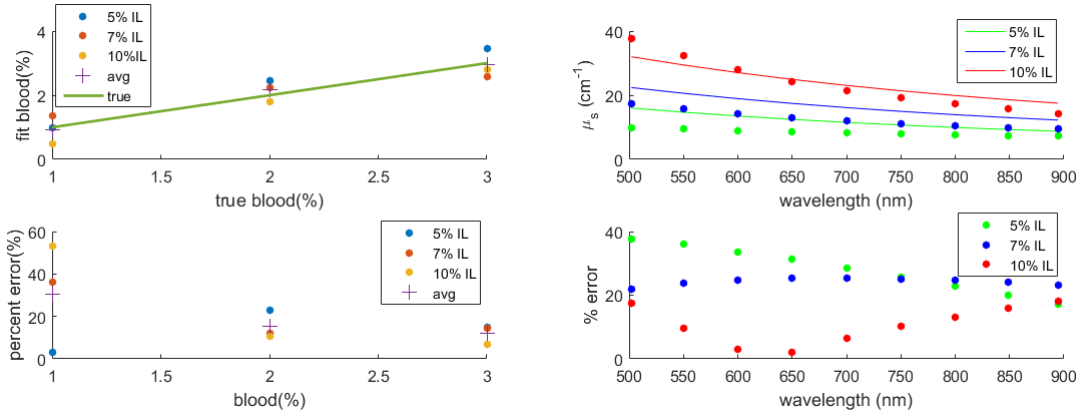

(a) *(b)*

Fig. 4.17 Results using DE for a probe with a SDS=2 mm. a) fitted values of whole blood concentration. b) μ_s fits and errors.

The fitting results of B% and μ_s of the phantoms using the DE are shown in Figure 4.17. The calibration factors evaluated using the DE suggested that the DE would yield more

accurate values of μ_s when using the long SDS probe compared to MC, but the evaluation of B% would be more or less the same. These hypotheses based on the calibration factors are verified in Figure 4.17. The average percent error of the fitted values of B% is 19.3% using the DE and 21.2% using MC. Additionally, μ_s values are clearly better fit using the DE with no data point having a percent error greater than 40% (compared to percent errors of over 100% when using MC). From these results, it can be concluded that the DE performs better than the MC model for longer SDSs. Again, this could be due to worsening planar fittings of the MC look-up table with increasing SDSs.

Chapter 5

Conclusions and Outlook

This work has attempted to provide a thorough study of DRS. Specifically, the composition of tissue-mimicking phantoms has been deduced using DRS and two different forward models. The specific individual aims of this project were outlined in Section 1.3. Here, the results for each of these specific aims are summarised.

5.1 Measuring the penetration depth of light

The ultimate aim of this work is to develop an evaluation protocol for determining the chromophore composition of tumour tissue which in the future could be used as a simple and effective diagnostic tool during radionuclide therapy. Keeping this long-term aim in mind, the penetration depth of light in different types of tissue was simulated in order to determine the types of systems this setup could be used in. The results from these simulations show that the penetration depth increases with increasing wavelength[1] and SDS[2]. However, the penetration depth in any case is on the order of μm. Therefore, were this system to be used in clinical studies, it could potentially be used in evaluating the composition of surface skin tissue, etc.

5.2 Phantom preparation and calibration

The DRS setup used was a two spectrometer system which provided a unique method for real time calibration of any time dependent light source intensity fluctuations. Various calibrations

[1] 660: maximum wavelength simulated.
[2] 4 mm: maximum SDS simulated.

techniques were developed, however the final calibration technique developed involved calibration of the differences in the two spectrometer responses and calibration between theoretical (FM) and experimental spectra using one calibration factor. These calibration factors were calculated using the data from the different liquid phantoms. Unexpectedly, these calibration factors changed depending on the properties of the liquid phantoms. This immediately suggests an error in either the optical properties of the phantoms, the model, or the set-up. These possible sources of error will now be summarised.

The optical properties of the phantoms were verified through transmission measurements, and are considered to be accurate. However, in order to be completely sure that the values of μ_a do not affect the results, a more well characterised absorber such as Haemoglobin powder or India ink could be used.

The MC look up table contains possible flaws mainly because the MC look up table is simulated using a pencil source light beam rather than a finite, realistic beam. Another possible error in the MC look up table can be a poor planar fitting of the simulated reflectance values, especially for longer SDSs.

Finally, the SDS of the probes can be inaccurately cited which can affect the FM spectrum. The set-up could be improved to give better calibration factors by using a more intense light source and a more sensitive spectrometer. This has been discussed in the results when looking at phantoms with high blood concentrations.

5.3 Evaluating phantom composition

Despite the problems seen in the calibration factors, the results obtained for the fitting of B% and [HHb]+[HbO_2] using MC and the short SDS probe are close to their true values. The DE yields less accurate values, which is expected from the theory. The individual concentrations of HHb and HbO_2 were not well-evaluated for the phantoms with high concentrations of blood (8 and 10%). However this can be improved using more sensitive equipment. The probe with a long SDS yielded fits with slightly lower average percent errors compared to the short probe when using MC. This strengthens the idea that convolution of the look-up table will produce better fits.

5.4 Outlook

The results obtained in this work suggest a promising outlook for using DRS in connection with evaluating tissue composition. There are still improvements that must be made, espe-

cially within convolution of the MC look-up table. Work on carrying out the convolution has been started, however the results are still in their initial stages. Finally, in order to make the experimental set-up more robust and capable of evaluating tissue with high absorber concentrations, more sensitive equipment should be used.

Not included in this thesis are the results of oxygenation studies. For the oxygenation studies, the liquid phantoms were deoxygenated by bubbling N_2 gas into the phantoms. Then, O_2 was carefully bubbled into the phantoms to increase their SO_2 values. The reflectance spectra of the phantoms with different SO_2 values were taken. The idea was then to see whether changes in SO_2 values could be evaluated. Although the data have been taken, the results could not be evaluated well due to the fact that the liquid phantoms used for this study contained low blood concentrations which, due to the calibration factors, could not be evaluated well. In the future, after the calibration factors have been corrected, it would be interesting to look at the results of this type of oxygenation study.

To complete this work, in-vivo studies on real biological systems must be carried out. These studies would verify how well the evaluation protocol could be used in a clinical setting. For now, only homogeneous liquid phantoms have been studied. In order to adapt the evaluation protocol to a real biological system, some changes to the existing protocol will probably need to be added. These changes would include modelling any vascular structure of tissue, as well as adding any chromophores that would likely be found in tissue (e.g. kerotin, etc.).

Bibliography

[1] WHO. Cancer: Fact sheet 297, 2015.

[2] Cancerfonden. Aktuell statistik om cancer, 2013.

[3] C. Hoefnagel. Radionuclide cancer therapy. *Ann. Nucl. Med.*, 12(2), 1998.

[4] Labsphere. Spectralon diffuse reflectance material, 2016.

[5] A. Giaccia E. Hall. Radiobiology for the radiologist.

[6] S Kizaka-Kondoh et al. H Harada. Significance of hif-1-active cells in angiogenesis and radioresistance. *Oncogene*, 26:7508–7516, 2007.

[7] et.al K. Vishwanath, Y. Hong. Using optical spectroscopy to longitudinally monitor physiological changes within solid tumours. *Neoplasia*, 11, 2009.

[8] K. Chang K. Vishwanath, D. Klein. Quantitative optical spectroscopy can identify long-term local tumor control in irradiated murine head and neck xenografts. *J Biomed Opt*, 14, 2009.

[9] et.al S. Kanick, H. Hoogsteden. Integration of single-fiber reflectane spectroscopy into ultrasound-guide endoscopic lung cancer staging of mediastinal lymph nodes. *J Biomed Opt*, 11, 2010.

[10] H. Fu B. Yu and N. Ramanujam. Instrument independent diffuse reflectance spectroscopy. *J Biomed Opt*, 16(1), 2011.

[11] Y.S. Li et. al T.Y. Tseng, C.Y. Chen. Quantification of the optical properties of two-layered turbid media by simultaneously analyzing the spectral and spatial information of steady-state diffuse reflectance spectroscopy. *Biomed Opt Express*, 2(4), 2011.

[12] MK. Markey et. al R. Hennessy, SL. Lim. Monte carlo lookup table-based inverse model for extracting optical properties from tissue-simulating phantoms using diffuse reflectance spectroscopy. *J Biomed Opt*, 18(3), 2013.

[13] B. García Cámara. *On light scattering by nanoparticles with convention and non-conventional optical properties*. PhD thesis, Universidad de Cantabria.

[14] L. Henyey and J. Greenstein. Diffuse radiation in the galaxy. *Astrophys. J.*, 93:70–83, 1941.

[15] S. Jaques and S. Prahl. Modeling optical and thermal distributions in tissue during laser irradiation. *Lasers Surg Med*, 6, 1987.

[16] S. Jacques. Optical properties of biological tissues: a review. *Physics in Medicine and Biology*, 58, 2013.

[17] T. Gersten. Hematocrit, 2003.

[18] P. Aruna A.M.K. Enejder, J. Swartling and S. Andersson-Engels. Influence of cell shape and aggregate formation on the optical properties of flowing whole blood. *Appl Opt*, 42(7), 2003.

[19] M.F. Perutz. Hemoglobin structure and respiratory transport. *Sci Am*, 239(6), 1978.

[20] R. Callister. Methemoglobin: Its causes and effects on pulmonary function and spo2 readings, 2003.

[21] F.R. Rannou G. Alexandrakis and A.F. Chatziioannou. Tomographic bioluminescence imaging by use of a combined optical-pet (opet) system: a computer simulation feasibility study. *Phys. Med. Biol.*, 50, 2005.

[22] M. Voort et. al R. Nachabe, B. Hendriks. Estimation of biological chromophores using diffuse optical spectroscopy: benefit of extending the uv-vis wavelength range to include 1000 to 1600 nm. *Opt Express*, 18(24), 2010.

[23] W.B. Baker T. Durduran, R. Choe and A.G. Yodh. Diffuse optics for tissue monitoring and tomography. *IOP Publishing: Reports on Progress in Physics*, 73, 2010.

[24] T. Farrell and M. Patterson. A diffusion theory model of spatially resolved, steady-state diffuse reflectance for the noninvasive determination of tissue optical properties in vivo. *Am. Assoc. Phys. Med*, 19(4), 1992.

[25] A. Desjardins et. al R. Nachabe, B. Hendriks. Estimation of lipid and water concentrations in scattering media with diffuse optical spectroscopy from 900 to 1600 nm. *J Biomed Opt*, 15(3), 2010.

[26] M. Larsson I. Fredriksson and T. Strömberg. Inverse monte carlo method in a multilayered tissue model for diffuse reflectance spectroscopy. *J Biomed Opt*, 17(4), 2012.

[27] Q. Liu and N.Ramanujam. Scaling method for fast monte carlo simulation of diffuse reflectance spectra from multilayered turbid media. *J. Opt. Soc. Am. A*, 24(7), 2007.

[28] F. Mul et.al R. Graaf, M. Koeling. Condensed monte carlo simulations for the description of light transport. *Appl. Opt.*, 32, 1993.

[29] Q. Fang D. Cappon, T. Farrell and J. Hayward. Fiber-optic probe design and optical property recovery algorithm for optical biopsy of brain tissue. *J Biomed Opt*, 18(10), 2013.

[30] S.L. Jacques L.H. Wang and L.Q. Zheng. Mcml-monte carlo modeling of photon transport in multi-layered tissues. *Comput Methods Programs Biomed*, 47:131–146, 1995.

[31] S. Roweis. Levenberg-marquardt optimization.

[32] S.L. Jacques L.H. Wang and L.Q. Zheng. Conv-convolution for responses to a finite diameter photon beam incident on multi-layered tissues. *Comput Methods Programs Biomed*, 50:141–150, 1997.

[33] S. Andersson-Engles E. Alerstam, T. Svensson. Parallel computing with graphics processing units for high-speed monte carlo simulation of photon migration. *J. Biomedical Optics Letters*, 13, 2008.

[34] J. van Marle et.al H. van Staveren, C. Moes. Light scattering in intralipid-10% in the wavelength range of 400-1100 nm. *Appl Opt*, 30:4507–4514, 1991.

[35] R. Nossal G.H. Weiss and R.F. Bonner. Statistics of penetration depth of photons re-emitted from irradiated tissue. *J Mod Opt*, 36:3:349–359, 1989.

[36] P.Platonov et.al J. Swartling, S. Pålsson. Changes in tissue optical properties due to radio-frequency ablation of myocardium. *Med Bio Engl Comp*, 41(4), 2003.

[37] F. Foschum R. Michels and A. Kienle. Optical properties of fat emulsions. *Opt Express*, 16:8:5907–5925, 2008.